

1 **ELASTIC WAVE PROPAGATION IN CURVILINEAR COORDINATES WITH MESH
2 REFINEMENT INTERFACES BY A FOURTH ORDER FINITE DIFFERENCE
3 METHOD**

4 LU ZHANG*, SIYANG WANG†, AND N. ANDERS PETERSSON‡

5 **Abstract.** We develop a fourth order accurate finite difference method for the three dimensional elastic wave equation
6 in isotropic media with the piecewise smooth material property. In our model, the material property can be discontinuous at
7 curved interfaces. The governing equations are discretized in second order form on curvilinear meshes by using a fourth order
8 finite difference operator satisfying a summation-by-parts property. The method is energy stable and high order accurate.
9 The highlight is that mesh sizes can be chosen according to the velocity structure of the material so that computational
10 efficiency is improved. At the mesh refinement interfaces with hanging nodes, physical interface conditions are imposed
11 by using ghost points and interpolation. With a fourth order predictor-corrector time integrator, the fully discrete scheme
12 is energy conserving. Numerical experiments are presented to verify the fourth order convergence rate and the energy
13 conserving property.

14 **Key words.** Elastic wave equations, Three space dimension, Finite difference methods, Summation-by-parts, Non-
15 conforming mesh refinement

16 **AMS subject classifications.** 65M06, 65M12

17 **1. Introduction.** Seismic wave propagation has important applications in earthquake simulation,
18 energy resources exploration, and underground motion analysis. In many practical problems, wave motion
19 is governed by the three dimensional (3D) anisotropic elastic wave equations. The layered structure of
20 the Earth gives rise to a piecewise smooth material property with discontinuities at internal interfaces,
21 which are often curved in realistic models. Because of the heterogeneous material property and internal
22 interfaces, the governing equations cannot be solved analytically, and it is necessary to use advanced
23 numerical techniques to solve the seismic wave propagation problem.

24 When solving hyperbolic partial differential equations (PDEs), for computational efficiency, it is
25 essential that the numerical methods are high order accurate (higher than second order). This is because
26 high order methods have much smaller dispersion error than lower order methods [4, 5]. However, it is
27 challenging to obtain a stable and high order accurate method in the presence of discontinuous material
28 property and non-trivial geometry.

29 Traditionally, the governing equations of seismic wave propagation are solved as a first order system,
30 either in velocity-strain or velocity-stress formulation, which consists of nine equations. With the finite
31 difference method, staggered grids are often used for first order systems, and recently the technique has
32 been generalized to staggered curvilinear grids for the wave equation [9].

33 In this paper, we use another approach that discretizes the governing equations in second order form.
34 Comparing with nine PDEs in a first order system, the second order formulation consists of only three
35 PDEs in the displacement variables. In many cases, this could be a more efficient approach in terms
36 of accuracy and memory usage. For spatial discretization, we consider the finite difference operators
37 constructed in [12] that satisfy a summation-by-parts (SBP) principle, which is a discrete analogue of
38 the integration-by-parts principle and is an important ingredient to obtain energy stability. The SBP
39 operators in [12] use a ghost point outside each boundary to impose boundary conditions strongly. It is
40 also possible to impose boundary conditions in a weak sense [2] by using the SBP operators constructed
41 in [8], which do not use any ghost point.

42 In the SBP finite difference framework, a multi-block approach is often taken when the material
43 property is discontinuous. That is, the domain is divided into subdomains such that the internal in-
44 terfaces are aligned with the material discontinuities. SBP operators are then used independently in
45 each subdomain for the spatial discretization of the governing equations. To patch subdomains together,
46 physical interface conditions are imposed at internal interfaces [1, 3]. It is challenging to derive energy

*Department of Mathematics, Southern Methodist University, Dallas, TX 75275, USA. Email: luzhang@smu.edu

†Division of Applied Mathematics, UKK, Mälardalen University, Västerås, Sweden. Email: siyang.wang@mdh.se

‡Center for Applied Scientific Computing, Lawrence Livermore National Laboratory, Livermore, CA 94551, USA. Email: petersson1@llnl.gov

47 stable interface coupling with high order accuracy.

48 In [11], a fourth order SBP finite difference method was developed to solve the 3D elastic wave
 49 equation in heterogeneous smooth media, where topography in non-rectangular domains is resolved by
 50 using curvilinear meshes. The main objective of the present paper is to develop a fourth order method
 51 that solves the governing equations in piecewise smooth media, where material discontinuities occur at
 52 curved interfaces. This is motivated by the fact that in realistic models, material properties are only
 53 piecewise smooth with discontinuities, and it is important to obtain high order accuracy even at the
 54 material interfaces. A highlight of our method is that mesh sizes in each subdomain can be chosen
 55 according to the velocity structure of the material property. This leads to difficulties of mesh refinement
 56 interfaces, but maximizes computational efficiency. In the context of seismic wave propagation, as going
 57 deeper in the Earth, the wave speed gets larger and the wavelength gets longer. Correspondingly, in
 58 our model, the mesh becomes coarser with increasing depth. In this way, the number of grid points per
 59 wavelength can be kept almost the same in the entire domain.

60 In [17], we developed a fourth order finite difference method for the 2D wave equations with mesh
 61 refinement interfaces on Cartesian grids. Our current work generalizes to 3D elastic wave equations on
 62 curvilinear grids. In a 3D domain, the material interfaces are 2D curved faces. To impose interface
 63 conditions on hanging nodes, we construct fourth order interpolation and restriction operators for 2D
 64 grid functions. These operators are compatible with the underlying finite difference operators. With a
 65 fourth order predictor-corrector time integrator, the fully discrete discretization is energy conserving.

66 The rest of the paper is organized as follows. In Sec. 2, we introduce the governing equations in
 67 curvilinear coordinates. The spatial discretization is presented in detail in Sec. 3. Particular emphasis is
 68 placed on the numerical coupling procedure at curved mesh refinement interfaces. In Sec. 4, we describe
 69 the temporal discretization and present the fully discrete scheme. Numerical experiments are presented in
 70 Sec. 5 to verify the convergence rate of the proposed scheme and the energy conserving property. We also
 71 demonstrate that the mesh refinement interfaces do not introduce spurious wave reflections. Conclusions
 72 are drawn in Sec. 6.

73 **2. The anisotropic elastic wave equation.** We consider the time dependent anisotropic elastic
 74 wave equation in a three dimensional domain $\mathbf{x} \in \Omega$, where $\mathbf{x} = (x^{(1)}, x^{(2)}, x^{(3)})^T$ are the Cartesian
 75 coordinates. The domain Ω is partitioned into two subdomains Ω^f and Ω^c , with an interface $\Gamma = \Omega^f \cap \Omega^c$.
 76 The material property is assumed to be smooth in each subdomain, but may be discontinuous at the
 77 interface Γ . Without loss of generality, we may assume that the wave speed is slower in Ω^f than in
 78 Ω^c , which motivates us to use a fine mesh in Ω^f and a coarse mesh in Ω^c . We further assume that
 79 both Ω^f and Ω^c have six, possibly curved boundary faces. Denote $\mathbf{r} = (r^{(1)}, r^{(2)}, r^{(3)})^T$, the parameter
 80 coordinates, and introduce smooth one-to-one mappings

$$81 \quad (2.1) \quad \mathbf{x} = \mathbf{X}^f(\mathbf{r}) : [0, 1]^3 \rightarrow \Omega^f \subset \mathbb{R}^3 \quad \text{and} \quad \mathbf{x} = \mathbf{X}^c(\mathbf{r}) : [0, 1]^3 \rightarrow \Omega^c \subset \mathbb{R}^3.$$

82 Let the inverse of the mappings in (2.1) be $\mathbf{r} = \mathbf{R}^f(\mathbf{x})$ with components $\mathbf{R}^f(\mathbf{x}) = (R^{f,(1)}, R^{f,(2)}, R^{f,(3)})^T$
 83 and $\mathbf{r} = \mathbf{R}^c(\mathbf{x})$ with components $\mathbf{R}^c(\mathbf{x}) = (R^{c,(1)}, R^{c,(2)}, R^{c,(3)})^T$, respectively. Note that we do not
 84 compute the components of the inverse mapping \mathbf{R}^c and \mathbf{R}^f in this paper, the definitions here are for
 85 the convenience of the rest of the contents.

86 We further assume that the interface Γ corresponds to $r^{(3)} = 1$ for the coarse domain and $r^{(3)} = 0$
 87 for the fine domain. Then the elastic wave equation in the coarse domain Ω^c in terms of the displacement
 88 vector $\mathbf{C} = \mathbf{C}(\mathbf{r}, t)$ can be written in curvilinear coordinates as (see [11])

$$89 \quad (2.2) \quad \rho^c \frac{\partial^2 \mathbf{C}}{\partial^2 t} = \frac{1}{J^c} [\bar{\partial}_1(A_1^c \nabla_r \mathbf{C}) + \bar{\partial}_2(A_2^c \nabla_r \mathbf{C}) + \bar{\partial}_3(A_3^c \nabla_r \mathbf{C})], \quad \mathbf{r} \in [0, 1]^3, \quad t \geq 0,$$

91 where ρ^c is the density function in the coarse domain Ω^c . We define

$$92 \quad A_k^c \nabla_r \mathbf{C} = \sum_{j=1}^3 N_{kj}^c \bar{\partial}_j \mathbf{C}, \quad k = 1, 2, 3,$$

94 with $\nabla_r = (\bar{\partial}_1, \bar{\partial}_2, \bar{\partial}_3)^T$, $\bar{\partial}_i = \frac{\partial}{\partial r^{(i)}}$, for $i = 1, 2, 3$ and

$$95 \quad (2.3) \quad N_{ij}^c = J^c O_i^T M_{ij}^c O_j, \quad i, j = 1, 2, 3,$$

96 where,

$$97 \quad O_1^T = \begin{pmatrix} 1 & 0 & 0 & 0 & 0 & 0 \\ 0 & 0 & 0 & 0 & 0 & 1 \\ 0 & 0 & 0 & 0 & 1 & 0 \end{pmatrix}, \quad O_2^T = \begin{pmatrix} 0 & 0 & 0 & 0 & 0 & 1 \\ 0 & 1 & 0 & 0 & 0 & 0 \\ 0 & 0 & 0 & 1 & 0 & 0 \end{pmatrix}, \quad O_3^T = \begin{pmatrix} 0 & 0 & 0 & 0 & 1 & 0 \\ 0 & 0 & 0 & 1 & 0 & 0 \\ 0 & 0 & 1 & 0 & 0 & 0 \end{pmatrix},$$

98 and M_{ij}^c are the symmetric and positive definite 6×6 stiffness matrices. In particular, for the isotropic
99 elastic wave equation, we have

$$100 \quad M_{11}^c = \begin{pmatrix} 2\mu^c + \lambda^c & 0 & 0 \\ 0 & \mu^c & 0 \\ 0 & 0 & \mu^c \end{pmatrix}, \quad M_{12}^c = \begin{pmatrix} 0 & \lambda^c & 0 \\ \mu^c & 0 & 0 \\ 0 & 0 & 0 \end{pmatrix},$$

101

$$102 \quad (2.4) \quad M_{22}^c = \begin{pmatrix} \mu^c & 0 & 0 \\ 0 & 2\mu^c + \lambda^c & 0 \\ 0 & 0 & \mu^c \end{pmatrix}, \quad M_{13}^c = \begin{pmatrix} 0 & 0 & \lambda^c \\ 0 & 0 & 0 \\ \mu^c & 0 & 0 \end{pmatrix},$$

103

$$104 \quad M_{33}^c = \begin{pmatrix} \mu^c & 0 & 0 \\ 0 & \mu^c & 0 \\ 0 & 0 & 2\mu^c + \lambda^c \end{pmatrix}, \quad M_{23}^c = \begin{pmatrix} 0 & 0 & 0 \\ 0 & 0 & \lambda^c \\ 0 & \mu^c & 0 \end{pmatrix},$$

105

$$106 \quad M_{31}^c = (M_{13}^c)^T, \quad M_{32}^c = (M_{23}^c)^T, \quad M_{21}^c = (M_{12}^c)^T.$$

107 Here, λ^c and μ^c are the first and second Lamé parameters, respectively.

108 From (2.3) we find that even in the isotropic case the matrices N_{ij}^c are full. Hence, wave propagation
109 in isotropic media has anisotropic properties in curvilinear coordinates. In both isotropic and anisotropic
110 material, the matrices N_{ii}^c , $i = 1, 2, 3$, are symmetric positive definite and $N_{ij}^c = (N_{ji}^c)^T$, $i, j = 1, 2, 3$.

111 Last, J^c is the Jacobian of the coordinate transformation with

$$112 \quad J^c = \det(\bar{\partial}_1 \mathbf{X}^c, \bar{\partial}_2 \mathbf{X}^c, \bar{\partial}_3 \mathbf{X}^c) \in (0, \infty).$$

113 Denote the unit outward normal $\mathbf{n}_i^{c,\pm} = (n_i^{c,\pm,1}, n_i^{c,\pm,2}, n_i^{c,\pm,3})$, $i = 1, 2, 3$, for the boundaries of the
114 subdomain Ω^c , then

$$115 \quad (2.5) \quad \mathbf{n}_i^{c,\pm} = \pm \frac{\nabla_x R^{c,(i)}}{|\nabla_x R^{c,(i)}|}.$$

117 Here, $\nabla_x = (\partial_1, \partial_2, \partial_3)^T$, $\partial_i = \frac{\partial}{\partial x^{(i)}}$, $i = 1, 2, 3$. Here, '+' corresponds to $r^{(i)} = 1$ and '-' corresponds
118 to $r^{(i)} = 0$. The relation between covariant basis vectors $\bar{\partial}_i \mathbf{X}^c$, $i = 1, 2, 3$ and contravariant basis vectors
119 $\nabla_x R^{c,(i)}$, $i = 1, 2, 3$ can be found in [11, 14]. The elastic wave equation in curvilinear coordinates for the
120 fine domain in terms of the displacement vector $\mathbf{F} = \mathbf{F}(\mathbf{r}, t)$ is defined in the same way as in the coarse
121 domain. We have

$$122 \quad (2.6) \quad \rho^f \frac{\partial^2 \mathbf{F}}{\partial^2 t} = \frac{1}{J^f} \left[\bar{\partial}_1 (A_1^f \nabla_r \mathbf{F}) + \bar{\partial}_2 (A_2^f \nabla_r \mathbf{F}) + \bar{\partial}_3 (A_3^f \nabla_r \mathbf{F}) \right], \quad \mathbf{r} \in [0, 1]^3, \quad t \geq 0.$$

124 At the interface Γ , suitable physical interface conditions are the continuity of the traction vectors
125 and the continuity of the displacement vectors,

$$126 \quad (2.7) \quad \frac{A_3^c \nabla_r \mathbf{C}}{J^c |\nabla_x R^{c,(3)}|} = \frac{A_3^f \nabla_r \mathbf{F}}{J^f |\nabla_x R^{f,(3)}|}, \quad \mathbf{F} = \mathbf{C}.$$

127 Together with suitable physical boundary conditions, the problem (2.2, 2.6) is well-posed [3, 11].

128 **3. The spatial discretization.** In this section, we describe the spatial discretization for the prob-
129 lem (2.2, 2.6, 2.7) and start with the SBP operators for the first and second derivative.

130 **3.1. SBP operators in 1D.** Consider a uniform discretization of the domain $x \in [0, 1]$ with the
 131 grids,

$$132 \quad \tilde{\mathbf{x}} = [x_0, x_1, \dots, x_n, x_{n+1}]^T, \quad x_i = (i-1)h, \quad i = 0, 1, \dots, n, n+1, \quad h = 1/(n-1),$$

133 where $i = 1, n$ correspond to the grid points at the boundary, and $i = 0, n+1$ are ghost points outside
 134 of the physical domain. The operator $D \approx \frac{\partial}{\partial x}$ is a first derivative SBP operator [6, 13] if

$$135 \quad (3.1) \quad (\mathbf{u}, D\mathbf{v})_h = -(D\mathbf{u}, \mathbf{v})_h - u_1 v_1 + u_n v_n,$$

136 with a scalar product

$$137 \quad (3.2) \quad (\mathbf{u}, \mathbf{v})_h = h \sum_{i=1}^n \omega_i u_i v_i.$$

138 Here, $0 < \omega_i < \infty$ are the weights of scalar product. The SBP operator D has a centered difference stencil
 139 at the grid points away from the boundary and the corresponding weights $\omega_i = 1$. To satisfy the SBP
 140 identity (3.1), the coefficients in D are modified at a few points near the boundary and the corresponding
 141 weights $\omega_i \neq 1$. The operator D does not use any ghost points. To discretize the elastic wave equation,
 142 we also need to approximate the second derivative with a variable coefficient $(\gamma(x)u_x)_x$. Here, the known
 143 function $\gamma(x) > 0$ describes the property of the material. There are two different fourth order accurate
 144 SBP operators for the approximation of $(\gamma(x)u_x)_x$. The first one $\tilde{G}(\gamma)\mathbf{u} \approx (\gamma(x)u_x)_x$, derived by Sjögren
 145 and Petersson [12], uses one ghost point outside each boundary, and satisfies the second derivative SBP
 146 identity,

$$147 \quad (3.3) \quad (\mathbf{u}, \tilde{G}(\gamma)\mathbf{v})_h = -S_\gamma(\mathbf{u}, \mathbf{v}) - u_1 \gamma_1 \tilde{\mathbf{b}}_1 \mathbf{v} + u_n \gamma_n \tilde{\mathbf{b}}_n \mathbf{v}.$$

148 Here, the symmetric positive semi-definite bilinear form $S_\gamma(\mathbf{u}, \mathbf{v}) = (Du, \gamma D\mathbf{v})_h + (\mathbf{u}, P(\gamma)\mathbf{v})_{hr}$ does not
 149 use any ghost points, $(\cdot, \cdot)_{hr}$ is a standard discrete scalar L^2 inner product. The positive semi-definite
 150 operator $P(\gamma)$ is small for smooth grid functions but non-zero for odd-even modes, see [11, 12] for details.

151 The operators $\tilde{\mathbf{b}}_1$ and $\tilde{\mathbf{b}}_n$ take the form

$$152 \quad (3.4) \quad \tilde{\mathbf{b}}_1 \mathbf{v} = \frac{1}{h} \sum_{i=0}^4 \tilde{d}_i v_i, \quad \tilde{\mathbf{b}}_n \mathbf{v} = \frac{1}{h} \sum_{i=n-3}^{n+1} \tilde{d}_i v_i.$$

153 They are fourth order approximations of the first derivative v_x on the left and right boundaries, respectively.
 154 We note that the notation $\tilde{G}(\gamma)\mathbf{v}$ implies that the operator \tilde{G} uses \mathbf{v} on all grid points $\tilde{\mathbf{x}}$, but
 155 $\tilde{G}(\gamma)\mathbf{v}$ only returns values on the grid \mathbf{x} without ghost points. Therefore, when writing in matrix form,
 156 \tilde{G} is a rectangular matrix of size n by $n+2$.

157 In [17], a method was developed to convert the SBP operator $\tilde{G}(\gamma)$ to another SBP operator $G(\gamma)$
 158 which does not use any ghost point and satisfy

$$159 \quad (3.5) \quad (\mathbf{u}, G(\gamma)\mathbf{v})_h = -S_\gamma(\mathbf{u}, \mathbf{v}) - u_1 \gamma_1 \mathbf{b}_1 \mathbf{v} + u_n \gamma_n \mathbf{b}_n \mathbf{v},$$

160 where $S_\gamma(\cdot, \cdot)$ is symmetric positive semi-definite. Here, \mathbf{b}_1 and \mathbf{b}_n are also finite difference operators for
 161 the first derivative at the boundaries, and are constructed to fourth order accuracy. They take the form

$$162 \quad (3.6) \quad \mathbf{b}_1 \mathbf{v} = \frac{1}{h} \sum_{i=1}^5 d_i v_i, \quad \mathbf{b}_n \mathbf{v} = \frac{1}{h} \sum_{i=n-4}^n d_i v_i.$$

163 In this case, $G(\gamma)$ is square in matrix form. We note that in [8], Mattsson constructed a similar SBP
 164 operator with a third order approximation of the first derivative at the boundaries.

165 For the second derivative SBP operators $\tilde{G}(\gamma)$ in (3.3) and $G(\gamma)$ in (3.5), both of them use a fourth
 166 order five points centered difference stencil to approximate $(\gamma u_x)_x$ at the interior points away from the
 167 boundaries. For the first and the last six grid points close to the boundaries, the operators $G(\gamma)$ and
 168 $\tilde{G}(\gamma)$ use second order accurate one-sided difference stencils. They are designed to satisfy (3.5) and (3.3),
 169 respectively.

170 In the following section, we use a combination of two SBP operators, $\tilde{G}(\gamma)$ and $G(\gamma)$, to develop a
 171 multi-block finite difference discretization for the elastic wave equation. The first SBP operator is $\tilde{G}(\gamma)$
 172 with ghost point, and the second SBP operator $G(\gamma)$, converted from $\tilde{G}(\gamma)$, does not use ghost point.

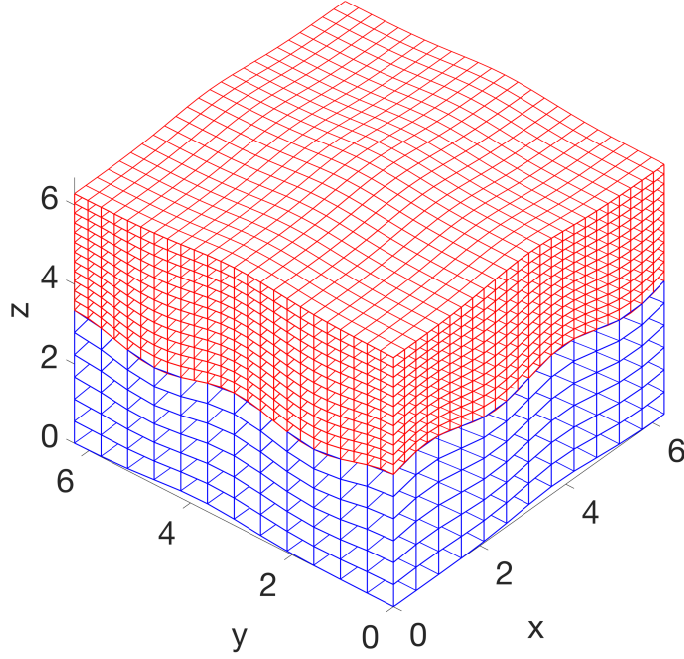


FIG. 1. The sketch for the curvilinear mesh of the physical domain Ω . The blue region is the spatial discretization of coarse subdomain Ω^c and the red region is the spatial discretization of the fine domain Ω^f . Note that x, y, z in the graph correspond to $x^{(1)}, x^{(2)}, x^{(3)}$ respectively.

3.2. Semi-discretization of the elastic wave equation. In this section, we discretize the elastic

wave equations (2.2) and (2.6) with mesh refinement interface Γ . We assume the ratio of mesh sizes in the reference domains is 1 : 2, that is the mesh sizes satisfy

$$h_1(n_1^h - 1) = 1, \quad h_2(n_2^h - 1) = 1, \quad h_3(n_3^h - 1) = 1,$$

and

$$2h_1(n_1^{2h} - 1) = 1, \quad 2h_2(n_2^{2h} - 1) = 1, \quad 2h_3(n_3^{2h} - 1) = 1.$$

Other ratios can be treated analogously. Figure 1 gives an illustration of the discretization of a physical domain. This is an ideal mesh if the wave speed in Ω^f is half of the wave speed in Ω^c .

In seismic wave simulation, far-field boundary conditions are often imposed in the $x^{(1)}$ and $x^{(2)}$ directions. Here, our focus is on the numerical treatment of the interface conditions (2.7). Therefore, we assume periodic boundary conditions in $x^{(1)}$ and $x^{(2)}$ and ignore the boundaries in $x^{(3)}$. In Figure 2, we fix $x^{(2)} = 0$ and present the $x^{(1)}\text{-}x^{(3)}$ section of the domain Ω in both curvilinear space and parameter space. To condense notations, we introduce the multi-index notations

$$\mathbf{i} = (i, j, k), \quad \mathbf{r}_i = (r_i^{(1)}, r_j^{(2)}, r_k^{(3)}), \quad \mathbf{x}_i = (x_i^{(1)}, x_j^{(2)}, x_k^{(3)}),$$

and group different sets of grid points according to

$$\begin{aligned} I_{\Omega^c} &= \{i = 1, 2, \dots, n_1^{2h}, j = 1, 2, \dots, n_2^{2h}, k = 1, 2, \dots, n_3^{2h}\}, \\ I_{\Gamma^c} &= \{i = 1, 2, \dots, n_1^{2h}, j = 1, 2, \dots, n_2^{2h}, k = n_3^{2h}\}, \\ I_{\Omega^f} &= \{i = 1, 2, \dots, n_1^h, j = 1, 2, \dots, n_2^h, k = 1, 2, \dots, n_3^h\}, \\ I_{\Gamma^f} &= \{i = 1, 2, \dots, n_1^h, j = 1, 2, \dots, n_2^h, k = 1\}. \end{aligned}$$

The physical coordinates of the coarse grid points and fine grid points follow from the mappings $\mathbf{x}_i = \mathbf{X}^c(\mathbf{r}_i)$ and $\mathbf{x}_i = \mathbf{X}^f(\mathbf{r}_i)$, respectively. We denote a grid function by

$$\mathbf{u}_i = \mathbf{u}_{i,j,k} = \mathbf{u}(\mathbf{x}_i),$$

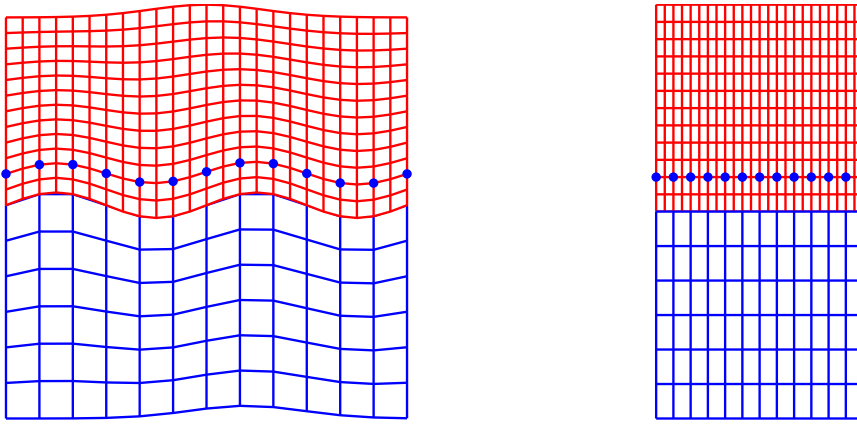


FIG. 2. The meshes in the physical domain (left) and parameter domain (right) of $x^{(1)}\text{-}x^{(3)}$ section with $x^{(2)} = 0$. The blue dots are the ghost points for the coarse domain Ω^c .

where \mathbf{u} can be either a scalar or vector. To distinguish between the continuous variables and the corresponding approximations on the grid, we use \mathbf{c}_i and \mathbf{f}_i to denote the grid functions for the approximations of $\mathbf{C}(\mathbf{x}_i)$ and $\mathbf{F}(\mathbf{x}_i)$, respectively. Let \mathbf{c} and \mathbf{f} be the vector representations of the grid functions \mathbf{c}_i and \mathbf{f}_i respectively. The elements of \mathbf{c} and \mathbf{f} are ordered in the following way:

- for each grid point \mathbf{x}_i , there is a 3×1 vector, say $\mathbf{c}_i = (c_i^{(1)}, c_i^{(2)}, c_i^{(3)})^T$ and $\mathbf{f}_i = (f_i^{(1)}, f_i^{(2)}, f_i^{(3)})^T$;
- the grid points are ordered such that they first loop over $r^{(1)}$ direction (i), then $r^{(2)}$ direction (j), and finally $r^{(3)}$ direction (k) as

$$\mathbf{c} = [c_{1,1,1}^{(1)}, c_{1,1,1}^{(2)}, c_{1,1,1}^{(3)}, c_{2,1,1}^{(1)}, c_{2,1,1}^{(2)}, c_{2,1,1}^{(3)}, \dots]^T, \quad \mathbf{f} = [f_{1,1,1}^{(1)}, f_{1,1,1}^{(2)}, f_{1,1,1}^{(3)}, f_{2,1,1}^{(1)}, f_{2,1,1}^{(2)}, f_{2,1,1}^{(3)}, \dots]^T.$$

We note that \mathbf{c} contains the ghost point values for $k = n_3^{2h} + 1$, but \mathbf{f} does not contain any ghost point values.

In the spatial discretization, we only use ghost points in the coarse domain and do not use ghost points in the fine domain. Comparing with the traditional approach of using ghost points in both domains, the system of linear equations at the interface becomes smaller and has a better structure. For the rest of the paper, the \sim over an operator represents that the operator applies to a grid function with ghost points. We approximate the elastic wave equation (2.2) in Ω^c by

$$(3.7) \quad \left((\rho^{2h} \otimes \mathbf{I})(J^{2h} \otimes \mathbf{I}) \frac{d^2 \mathbf{c}}{dt^2} \right)_i = \tilde{\mathcal{L}}_i^{2h} \mathbf{c}, \quad i \in I_{\Omega^c}, \quad t > 0,$$

where ρ^{2h} and J^{2h} are $n_1^{2h} n_2^{2h} n_3^{2h} \times n_1^{2h} n_2^{2h} n_3^{2h}$ diagonal matrices with the diagonal elements $\rho_i^{2h} = \rho^c(\mathbf{x}_i)$ and $J_i^{2h} = J^c(\mathbf{x}_i)$, $i \in I_{\Omega^c}$; the matrix \mathbf{I} is a 3×3 identity matrix because the spatial dimension of the governing equation is 3; finally, the discrete spatial operator is

$$(3.8) \quad \tilde{\mathcal{L}}^{2h} \mathbf{c} = \left(\sum_{l=1}^2 Q_l^{2h}(N_{ll}^{2h}) \mathbf{c} + \tilde{G}_3^{2h}(N_{33}^{2h}) \mathbf{c} + \sum_{l=1}^3 \sum_{m=1, m \neq l}^3 D_l^{2h}(N_{lm}^{2h} D_m^{2h} \mathbf{c}) \right),$$

which uses ghost points when compute $\tilde{G}_3^{2h}(N_{33}^{2h}) \mathbf{c}$. In Appendix A, the terms $Q_l^{2h}(N_{ll}^{2h}) \mathbf{c}$, $\tilde{G}_3^{2h}(N_{33}^{2h}) \mathbf{c}$ and $D_l^{2h}(N_{lm}^{2h} D_m^{2h} \mathbf{c})$ are presented, which approximate $\bar{\partial}_l(N_{ll} \bar{\partial}_l \mathbf{C})$, $\bar{\partial}_3(N_{33} \bar{\partial}_3 \mathbf{C})$ and $\bar{\partial}_l(N_{lm} \bar{\partial}_m \mathbf{C})$, respectively.

Next, we approximate the elastic wave equation (2.6) on the fine grid points. For all fine grid points that are not located at the interface Γ , the semi-discretization is

$$(3.9) \quad \left((\rho^h \otimes \mathbf{I})(J^h \otimes \mathbf{I}) \frac{d^2 \mathbf{f}}{dt^2} \right)_i = \mathcal{L}_i^h \mathbf{f}, \quad i \in I_{\Omega^f} \setminus I_{\Gamma^f}, \quad t > 0.$$

217 Here, ρ^h and J^h are $n_1^h n_2^h n_3^h \times n_1^h n_2^h n_3^h$ diagonal matrices with the diagonal elements $\rho_{\mathbf{i}}^h = \rho^f(\mathbf{x}_i)$ and
 218 $J_{\mathbf{i}}^h = J^f(\mathbf{x}_i)$, $\mathbf{i} \in I_{\Omega^f}$. And the discrete spatial operator is

219 (3.10)
$$\mathcal{L}^h \mathbf{f} = \left(\sum_{l=1}^2 Q_l^h(N_{ll}^h) \mathbf{f} + G_3^h(N_{33}^h) \mathbf{f} + \sum_{l=1}^3 \sum_{m=1, m \neq l}^3 D_l^h(N_{lm}^h D_m^h \mathbf{f}) \right).$$

220 Here, the term $G_3^h(N_{33}^h) \mathbf{f}$ approximating $\bar{\partial}_3(N_{33} \bar{\partial}_3 \mathbf{F})$ without using any ghost points is presented in
 221 Appendix A; the terms $Q_l^h(N_{ll}^h) \mathbf{f}$ and $D_l^h(N_{lm}^h D_m^h \mathbf{f})$ are defined similar as those in (3.8) and are used to
 222 approximate $\bar{\partial}_l(N_{ll} \bar{\partial}_l \mathbf{F})$ and $\bar{\partial}_l(N_{lm} \bar{\partial}_m \mathbf{F})$, respectively.

223 For the approximation at the interface Γ , we obtain the numerical solution using a scaled interpolation
 224 operator

225 (3.11)
$$\mathbf{f}_{\mathbf{i}} = \mathcal{P}_{\mathbf{i}}(\mathbf{c}), \quad \mathbf{i} \in I_{\Gamma^f},$$

226 which imposes the continuity of the solution at the interface Γ . For energy stability, the operator \mathcal{P} must
 227 be of a specific form

228 (3.12)
$$\mathcal{P} = \left((J_{\Gamma}^h \Lambda^h)^{-\frac{1}{2}} \mathbf{P} (J_{\Gamma}^{2h} \Lambda^{2h})^{\frac{1}{2}} \right) \otimes \mathbf{I}.$$

229 Here, J_{Γ}^h and Λ^h are $n_1^h n_2^h \times n_1^h n_2^h$ diagonal matrices with diagonal elements $J_{\Gamma, \mathbf{i}}^h = J^f(\mathbf{x}_i)$ and $\Lambda_{\mathbf{i}}^h =$
 230 $|\nabla_x R^{f,(3)}(\mathbf{x}_i)|$, $\mathbf{i} \in I_{\Gamma^f}$. Similarly, J_{Γ}^{2h} and Λ^{2h} are $n_1^{2h} n_2^{2h} \times n_1^{2h} n_2^{2h}$ diagonal matrices with diagonal
 231 elements $J_{\Gamma, \mathbf{i}}^{2h} = J^c(\mathbf{x}_i)$ and $\Lambda_{\mathbf{i}}^{2h} = |\nabla_x R^{c,(3)}(\mathbf{x}_i)|$, $\mathbf{i} \in I_{\Gamma^c}$. Finally, \mathbf{P} is an interpolation operator of size
 232 $n_1^h n_2^h \times n_1^{2h} n_2^{2h}$ for scalar grid functions at Γ^c . Since the spatial discretization is fourth order accurate, we
 233 also use a fourth order interpolation. With mesh refinement ratio 1 : 2, the stencils \mathbf{P} have four cases as
 234 illustrated in Figure 3. Consequently, the scaled interpolation operator \mathcal{P} is also fourth order accurate.

235 In the implementation of our scheme, we use (3.11) to obtain the solution at the interface of the fine
 236 domain. However, in the energy analysis in Sec. 3.3, it is more convenient to use the equivalent form

237 (3.13)
$$\left((\rho^h \otimes \mathbf{I})(J^h \otimes \mathbf{I}) \frac{d^2 \mathbf{f}}{dt^2} \right)_{\mathbf{i}} = \mathcal{L}_{\mathbf{i}}^h \mathbf{f} + \boldsymbol{\eta}_{\mathbf{i}}, \quad \mathbf{i} \in I_{\Gamma^f}$$

238 with

239 (3.14)
$$\boldsymbol{\eta} = ((\rho^h J^h) \otimes \mathbf{I}) \mathcal{P} \left(((\rho^{2h} J^{2h}) \otimes \mathbf{I})^{-1} \tilde{\mathcal{L}}^{2h} \mathbf{c} \right) - \mathcal{L}^h \mathbf{f}.$$

240 The variable $\boldsymbol{\eta}$ in (3.14) is approximately zero with a second order truncation error, which is of the same
 241 order as the boundary stencil of the SBP operator. Hence, $\boldsymbol{\eta}$ does not affect the order of truncation
 242 error in the spatial discretization. For the simplicity of analysis, we introduce a general notation for the
 243 schemes (3.9) and (3.13) in the fine domain Ω^f ,

244 (3.15)
$$\left((\rho^h \otimes \mathbf{I})(J^h \otimes \mathbf{I}) \frac{d^2 \mathbf{f}}{dt^2} \right)_{\mathbf{i}} = \hat{\mathcal{L}}_{\mathbf{i}}^h \mathbf{f} = \begin{cases} \mathcal{L}_{\mathbf{i}}^h \mathbf{f} + \boldsymbol{\eta}_{\mathbf{i}}, & \mathbf{i} \in I_{\Gamma^f} \\ \mathcal{L}_{\mathbf{i}}^h \mathbf{f}, & \mathbf{i} \in I_{\Omega^f} \setminus I_{\Gamma^f} \end{cases} \quad t > 0.$$

246 The following condition imposes continuity of traction at the interface, the first equation in (2.7),

247 (3.16)
$$\left(((\Lambda^{2h} J_{\Gamma}^{2h}) \otimes \mathbf{I})^{-1} \tilde{\mathcal{A}}_3^{2h} \mathbf{c} \right)_{\mathbf{i}} = \mathcal{R}_{\mathbf{i}} \left(((\Lambda^h J_{\Gamma}^h) \otimes \mathbf{I})^{-1} (\mathcal{A}_3^h \mathbf{f} - h_3 \omega_1 \boldsymbol{\eta}) \right), \quad \mathbf{i} \in I_{\Gamma^c}.$$

248 Here, $((\Lambda^{2h} J_{\Gamma}^{2h}) \otimes \mathbf{I})^{-1} \tilde{\mathcal{A}}_3^{2h} \mathbf{c}$ and $((\Lambda^h J_{\Gamma}^h) \otimes \mathbf{I})^{-1} \mathcal{A}_3^h \mathbf{f}$ are approximations of the traction at the interface
 249 on the coarse grid and fine grid, respectively. The definitions of $\tilde{\mathcal{A}}_3^{2h} \mathbf{c}$ and $\mathcal{A}_3^h \mathbf{f}$ are given in Appendix A.
 250 The operator \mathcal{R} is a scaled restriction operator with the structure

251 (3.17)
$$\mathcal{R} = \left((J_{\Gamma}^{2h} \Lambda^{2h})^{-\frac{1}{2}} \mathbf{R} (J_{\Gamma}^h \Lambda^h)^{\frac{1}{2}} \right) \otimes \mathbf{I},$$

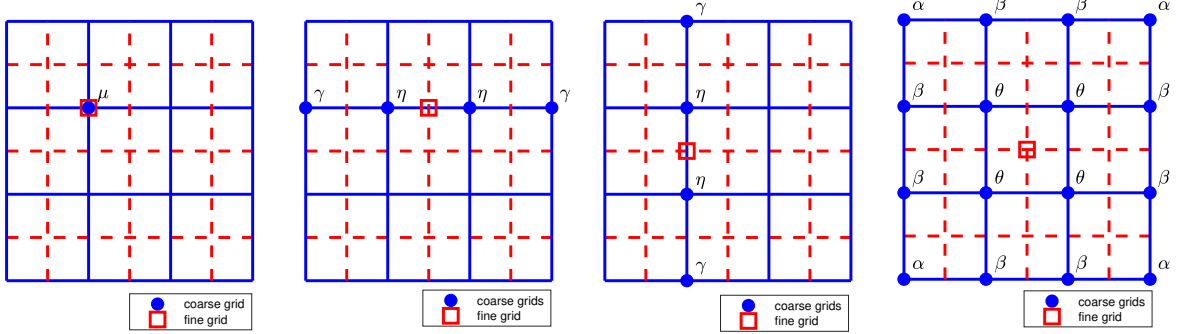


FIG. 3. The sketch for the stencils of fourth order interpolation operator \mathbf{P} in two dimensions with parameters $\gamma = -\frac{1}{16}$, $\eta = \frac{9}{16}$, $\mu = 1$, $\alpha = \frac{1}{256}$, $\beta = -\frac{9}{256}$ and $\theta = \frac{81}{256}$.

where the stencils of \mathbf{R} in Figure 4 are determined by the compatibility condition $\mathbf{R} = \frac{1}{4}\mathbf{P}^T$. It is a restriction operator of size $n_1^{2h}n_2^{2h} \times n_1^h n_2^h$ for scalar grid functions at Γ^f . Finally, $h_3\omega_1\boldsymbol{\eta}$ in (3.16) is a term essential for stability, because in the stability analysis in the next section it cancels out $\boldsymbol{\eta}$ in the fine domain spatial discretization (3.15). The term is smaller than the truncation error of spatial discretization, so it does not affect the overall order of truncation error. Hence, (3.16) is a sufficiently accurate approximation for the continuity of traction at the interface. As will be seen later, the compatibility condition, as well as the scaling of the interpolation and restriction operators, are important for energy stability [7]. We also remark that the condition (3.16) determines the ghost points values in the coarse domain.

Let \mathbf{u} and \mathbf{v} be grid functions in the coarse domain Ω^c . We define the discrete inner product at the interface by

$$(3.18) \quad \langle \mathbf{u}, \mathbf{v} \rangle_{2h} = 4h_1 h_2 \sum_{i=1}^{n_1^{2h}} \sum_{j=1}^{n_2^{2h}} J_{\Gamma, i, j, n_3^{2h}}^{2h} \Lambda_{i, j, n_3^{2h}}^{2h} (\mathbf{u}_{i, j, n_3^{2h}} \cdot \mathbf{v}_{i, j, n_3^{2h}}).$$

Similarly, the discrete inner product at the interface for fine domain Ω^f is defined as

$$(3.19) \quad \langle \mathbf{u}, \mathbf{v} \rangle_h = h_1 h_2 \sum_{i=1}^{n_1^h} \sum_{j=1}^{n_2^h} J_{\Gamma, i, j, 1}^h \Lambda_{i, j, 1}^h (\mathbf{u}_{i, j, 1} \cdot \mathbf{v}_{i, j, 1})$$

when \mathbf{u} and \mathbf{v} are grid functions in fine domain Ω^f . Then we have the following lemma for the interpolation and restriction operators.

LEMMA 3.1. Let \mathbf{c} and \mathbf{f} be grid functions at the interface for coarse domain and fine domain, respectively. Then the interpolation operator \mathcal{P} and the restriction operator \mathcal{R} satisfy

$$(3.20) \quad \langle \mathcal{P}\mathbf{c}, \mathbf{f} \rangle_h = \langle \mathbf{c}, \mathcal{R}\mathbf{f} \rangle_{2h}$$

if the compatibility condition $\mathbf{R} = \frac{1}{4}\mathbf{P}^T$ holds.

Proof. From (3.18)–(3.19), the definition of \mathcal{P} in (3.12) and \mathcal{R} in (3.17), we obtain

$$\begin{aligned} \langle \mathcal{P}\mathbf{c}, \mathbf{f} \rangle_h &= h_1 h_2 \left[\left((J_{\Gamma}^h \Lambda^h)^{\frac{1}{2}} \mathbf{P} (J_{\Gamma}^{2h} \Lambda^{2h})^{\frac{1}{2}} \otimes \mathbf{I} \right) \mathbf{c} \right]^T \mathbf{f} \\ &= 4h_1 h_2 \mathbf{c}^T \left[\left((J_{\Gamma}^{2h} \Lambda^{2h})^{\frac{1}{2}} \frac{1}{4} \mathbf{P}^T (J_{\Gamma}^h \Lambda^h)^{\frac{1}{2}} \otimes \mathbf{I} \right) \mathbf{f} \right] \\ &= 4h_1 h_2 \mathbf{c}^T \left[\left((J_{\Gamma}^{2h} \Lambda^{2h})^{\frac{1}{2}} \mathbf{R} (J_{\Gamma}^h \Lambda^h)^{\frac{1}{2}} \otimes \mathbf{I} \right) \mathbf{f} \right] = \langle \mathbf{c}, \mathcal{R}\mathbf{f} \rangle_{2h} \end{aligned} \quad \square$$

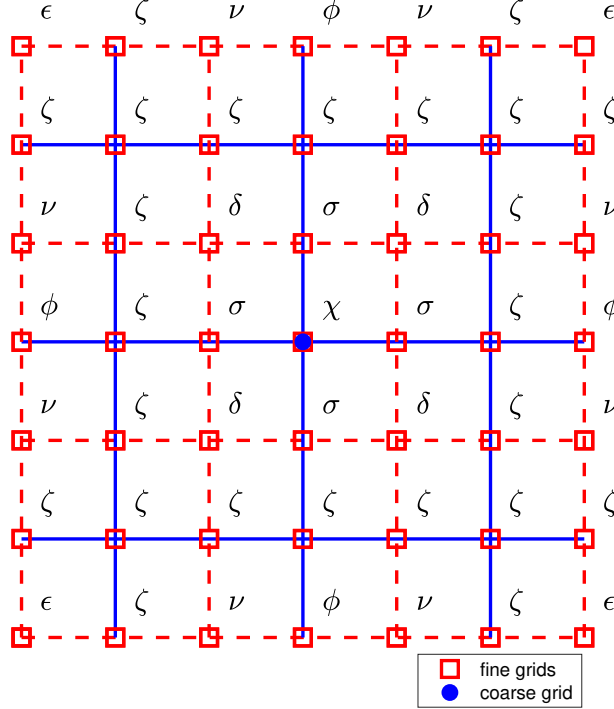


FIG. 4. The sketch for the stencil of fourth order restriction operator \mathbf{R} in two dimensions with parameters $\epsilon = \frac{1}{1024}$, $\nu = -\frac{9}{1024}$, $\phi = -\frac{16}{1024}$, $\delta = \frac{81}{1024}$, $\sigma = \frac{144}{1024}$, $\chi = \frac{256}{1024}$ and $\zeta = 0$.

276 **3.3. Energy estimate.** In this section, we derive an energy estimate for the semi-discretization
 277 (3.7) and (3.15) in Sec. 3.2. Let \mathbf{u}, \mathbf{v} be grid functions in the coarse domain Ω^c and define the three
 278 dimensional discrete scalar product in Ω^c as

$$279 \quad (3.21) \quad (\mathbf{v}, \mathbf{u})_{2h} = 8h_1 h_2 h_3 \sum_{i=1}^{n_1^{2h}} \sum_{j=1}^{n_2^{2h}} \sum_{k=1}^{n_3^{2h}} \omega_k J_{i,j,k}^{2h} (\mathbf{v}_{i,j,k} \cdot \mathbf{u}_{i,j,k}).$$

280 Similarly, define the three dimensional discrete scalar product in Ω^f as

$$281 \quad (3.22) \quad (\mathbf{v}, \mathbf{u})_h = h_1 h_2 h_3 \sum_{i=1}^{n_1^h} \sum_{j=1}^{n_2^h} \sum_{k=1}^{n_3^h} \omega_k J_{i,j,k}^h (\mathbf{v}_{i,j,k} \cdot \mathbf{u}_{i,j,k}),$$

282 where \mathbf{u} and \mathbf{v} are grid functions in the fine domain Ω^f . Now, we are ready to state the energy estimate
 283 of the proposed schemes in Section 3.2.

284 THEOREM 3.2. *The semi-discretization (3.7) and (3.15) is energy stable if the interface conditions
 285 (3.11) and (3.16) are satisfied.*

286 *Proof.* Forming the inner product between (3.7) and $8h_1 h_2 h_3 \omega_k \mathbf{c}_t$, and summing over i, j, k , we have

$$287 \quad (3.23) \quad 8h_1 h_2 h_3 \sum_{i=1}^{n_1^{2h}} \sum_{j=1}^{n_2^{2h}} \sum_{k=1}^{n_3^{2h}} \omega_k \mathbf{c}_t \cdot \left((\rho^{2h} \otimes \mathbf{I})(J^{2h} \otimes \mathbf{I}) \frac{d^2 \mathbf{c}}{dt^2} \right) = 8h_1 h_2 h_3 \sum_{i=1}^{n_1^{2h}} \sum_{j=1}^{n_2^{2h}} \sum_{k=1}^{n_3^{2h}} \omega_k J_{i,j,k}^{2h} \mathbf{c}_t \cdot \left((\rho^{2h} \otimes \mathbf{I}) \frac{d^2 \mathbf{c}}{dt^2} \right)$$

$$288 \quad = (\mathbf{c}_t, (\rho^{2h} \otimes \mathbf{I}) \mathbf{c}_{tt})_{2h} = (\mathbf{c}_t, (J^{2h} \otimes \mathbf{I})^{-1} \tilde{\mathcal{L}}^{2h} \mathbf{c})_{2h} = -\mathcal{S}_{2h}(\mathbf{c}_t, \mathbf{c}) + B_{2h}(\mathbf{c}_t, \mathbf{c}),$$

289 where $\mathcal{S}_{2h}(\mathbf{c}_t, \mathbf{c})$ is a symmetric and positive definite bilinear form given in Appendix B, the boundary

290 term $B_{2h}(\mathbf{c}_t, \mathbf{c})$ is given by

291 (3.24)
$$B_{2h}(\mathbf{c}_t, \mathbf{c}) = 4h_1 h_2 \sum_{\mathbf{i} \in I_{\Gamma^c}} \frac{d\mathbf{c}_i}{dt} \cdot (\tilde{A}_3^{2h} \mathbf{c})_{\mathbf{i}}.$$

292 Forming the inner product between (3.15) and $h_1 h_2 h_3 \omega_k \mathbf{f}_t$, and summing over i, j, k , we obtain

293 (3.25)
$$\begin{aligned} h_1 h_2 h_3 \sum_{i=1}^{n_1^h} \sum_{j=1}^{n_2^h} \sum_{k=1}^{n_3^h} \omega_k \mathbf{f}_t \cdot \left((\rho^h \otimes \mathbf{I})(J^h \otimes \mathbf{I}) \frac{d^2 \mathbf{f}}{dt^2} \right) &= h_1 h_2 h_3 \sum_{i=1}^{n_1^h} \sum_{j=1}^{n_2^h} \sum_{k=1}^{n_3^h} \omega_k J_{i,j,k}^h \mathbf{f}_t \cdot \left((\rho^h \otimes \mathbf{I}) \frac{d^2 \mathbf{f}}{dt^2} \right) \\ &= (\mathbf{f}_t, (\rho^h \otimes \mathbf{I}) \mathbf{f}_{tt})_h = (\mathbf{f}_t, (J^h \otimes \mathbf{I})^{-1} \hat{\mathcal{L}}^h \mathbf{f})_h = -\mathcal{S}_h(\mathbf{f}_t, \mathbf{f}) + B_h(\mathbf{f}_t, \mathbf{f}) + h_1 h_2 h_3 \omega_1 \sum_{i=1}^{n_1^h} \sum_{j=1}^{n_2^h} \frac{d\mathbf{f}_{i,j,1}}{dt} \cdot \boldsymbol{\eta}_{i,j,1}. \end{aligned}$$

295 Here, \mathcal{S}_h is also a symmetric and positive definite bilinear form given in Appendix B. The boundary term
296 $B_h(\mathbf{f}_t, \mathbf{f})$ has the following form

297 (3.26)
$$B_h(\mathbf{f}_t, \mathbf{f}) = -h_1 h_2 \sum_{\mathbf{i} \in I_{\Gamma^f}} \frac{d\mathbf{f}_i}{dt} \cdot (A_3^h \mathbf{f})_{\mathbf{i}}.$$

298 Adding (3.23) and (3.25) together, we have

299 (3.27)
$$\begin{aligned} \frac{d}{dt} [(\mathbf{f}_t, (\rho^h \otimes \mathbf{I}) \mathbf{f}_t)_h + \mathcal{S}_h(\mathbf{f}, \mathbf{f}) + (\mathbf{c}_t, (\rho^{2h} \otimes \mathbf{I}) \mathbf{c}_t)_{2h} + \mathcal{S}_{2h}(\mathbf{c}, \mathbf{c})] &= \\ 300 &2B_h(\mathbf{f}_t, \mathbf{f}) + 2B_{2h}(\mathbf{c}_t, \mathbf{c}) + 2h_1 h_2 h_3 \omega_1 \sum_{i=1}^{n_1^h} \sum_{j=1}^{n_2^h} \frac{d\mathbf{f}_{i,j,1}}{dt} \cdot \boldsymbol{\eta}_{i,j,1}. \end{aligned}$$

301 302 Substituting (3.26) and (3.24) into (3.27) and combining the definitions of the scalar product at the
303 interface (3.18)–(3.19), the continuity of solution at the interface (3.11) and Lemma 3.1, we get

305
$$\begin{aligned} \frac{d}{dt} [(\mathbf{f}_t, (\rho^h \otimes \mathbf{I}) \mathbf{f}_t)_h + \mathcal{S}_h(\mathbf{f}, \mathbf{f}) + (\mathbf{c}_t, (\rho^{2h} \otimes \mathbf{I}) \mathbf{c}_t)_{2h} + \mathcal{S}_{2h}(\mathbf{c}, \mathbf{c})] \\ 306 &= 2 \langle \mathbf{f}_t, ((\Lambda^h J_{\Gamma}^h) \otimes \mathbf{I})^{-1} (-\mathcal{A}_3^h \mathbf{f} + h_3 \omega_1 \boldsymbol{\eta}) \rangle_h + 2 \langle \mathbf{c}_t, ((\Lambda^{2h} J_{\Gamma}^{2h}) \otimes \mathbf{I})^{-1} \tilde{\mathcal{A}}_3^{2h} \mathbf{c} \rangle_{2h} \\ 307 &= 2 \langle \mathcal{P} \mathbf{c}_t, ((\Lambda^h J_{\Gamma}^h) \otimes \mathbf{I})^{-1} (-\mathcal{A}_3^h \mathbf{f} + h_3 \omega_1 \boldsymbol{\eta}) \rangle_h + 2 \langle \mathbf{c}_t, ((\Lambda^{2h} J_{\Gamma}^{2h}) \otimes \mathbf{I})^{-1} \tilde{\mathcal{A}}_3^{2h} \mathbf{c} \rangle_{2h} \\ 308 &= 2 \langle \mathbf{c}_t, \mathcal{R}((\Lambda^h J_{\Gamma}^h) \otimes \mathbf{I})^{-1} (-\mathcal{A}_3^h \mathbf{f} + h_3 \omega_1 \boldsymbol{\eta}) \rangle_{2h} + 2 \langle \mathbf{c}_t, ((\Lambda^{2h} J_{\Gamma}^{2h}) \otimes \mathbf{I})^{-1} \tilde{\mathcal{A}}_3^{2h} \mathbf{c} \rangle_{2h} = 0. \end{aligned}$$

310 Note that the discrete energy for the semi-discretization (3.7) and (3.15) is given by $(\mathbf{f}_t, (\rho^h \otimes \mathbf{I}) \mathbf{f}_t)_h +$
311 $\mathcal{S}_h(\mathbf{f}, \mathbf{f}) + (\mathbf{c}_t, (\rho^{2h} \otimes \mathbf{I}) \mathbf{c}_t)_{2h} + \mathcal{S}_{2h}(\mathbf{c}, \mathbf{c})$. \square

312 **4. The temporal discretization.** The equations are advanced in time with an explicit fourth
313 order accurate predictor-corrector time integration method. Like all explicit time stepping methods, the
314 time step must not exceed the CFL stability limit. By a similar analysis as in [12], we require

315
$$\Delta_t \leq C_{\text{cfl}} \min\{h_1, h_2, h_3\} / \sqrt{\kappa_{\max}},$$

316 where $C_{\text{cfl}} = 1.3$ and κ_{\max} is the maximum eigenvalue of the matrices

317
$$T_{\mathbf{i}}^{\{f,c\}} = \frac{1}{\rho^{\{f,c\}}(\mathbf{r}_i)} \begin{pmatrix} Tr(N_{11}^{\{f,c\}}(\mathbf{r}_i)) & Tr(N_{12}^{\{f,c\}}(\mathbf{r}_i)) & Tr(N_{13}^{\{f,c\}}(\mathbf{r}_i)) \\ Tr(N_{21}^{\{f,c\}}(\mathbf{r}_i)) & Tr(N_{22}^{\{f,c\}}(\mathbf{r}_i)) & Tr(N_{23}^{\{f,c\}}(\mathbf{r}_i)) \\ Tr(N_{31}^{\{f,c\}}(\mathbf{r}_i)) & Tr(N_{32}^{\{f,c\}}(\mathbf{r}_i)) & Tr(N_{33}^{\{f,c\}}(\mathbf{r}_i)) \end{pmatrix},$$

318 319 where $Tr(N_{lm}^{\{f,c\}}(\mathbf{r}_i))$ represents the trace of 3×3 matrix $N_{lm}^{\{f,c\}}(\mathbf{r}_i)$. Note that κ_{\max} is related to the
material properties $\mu^{\{f,c\}}$, $\lambda^{\{f,c\}}$ and $\rho^{\{f,c\}}$. The notation $\{\cdot, \cdot\}$ represents the component-wise identities.

320 In the following, we give detailed procedures about how we apply the fourth order time integrator to the
 321 semidiscretizations (3.7) and (3.15).

322 Let \mathbf{c}^n and \mathbf{f}^n denote the numerical approximations of $\mathbf{C}(\mathbf{x}, t_n)$, $\mathbf{x} \in \Omega^c$ and $\mathbf{F}(\mathbf{x}, t_n)$, $\mathbf{x} \in \Omega^f$, respectively.
 323 Here, $t_n = n\Delta_t$, $n = 0, 1, \dots$ and $\Delta_t > 0$ is a constant time step. We present the fourth order
 324 time integrator with predictor and corrector in Algorithm 4.1.

325 **Algorithm 4.1** Fourth order accurate time stepping for the semidiscretizations (3.7) and (3.15).

327 Given $\tilde{\mathbf{c}}^n, \tilde{\mathbf{c}}^{n-1}$ and $\mathbf{f}^n, \mathbf{f}^{n-1}$ that satisfy the discretized interface conditions.

- 328 • Compute the predictor at the interior grid points

329
$$\mathbf{c}_i^{*,n+1} = 2\mathbf{c}_i^n - \mathbf{c}_i^{n-1} + \Delta_t^2 ((\rho^{2h} \otimes \mathbf{I})(J^{2h} \otimes \mathbf{I}))^{-1} \hat{\mathcal{L}}_i^{2h} \mathbf{c}^n, \quad i \in I_{\Omega^c},$$

330
$$\mathbf{f}_i^{*,n+1} = 2\mathbf{f}_i^n - \mathbf{f}_i^{n-1} + \Delta_t^2 ((\rho^h \otimes \mathbf{I})(J^h \otimes \mathbf{I}))^{-1} \hat{\mathcal{L}}_i^h \mathbf{f}^n, \quad i \in I_{\Omega^f} \setminus I_{\Gamma^f}.$$

- 332 • At the interface Γ , the values $\mathbf{f}_i^{*,n+1}$ are computed by the continuity of solution

333
$$\mathbf{f}_i^{*,n+1} = \mathcal{P}_i(\mathbf{c}_i^{*,n+1}), \quad i \in I_{\Gamma^f}.$$

- 334 • At the interface Γ , the ghost point values in $\tilde{\mathbf{c}}^{*,n+1}$ are computed by solving the equation for the
 335 continuity of traction

336 (4.1)
$$\left(((\Lambda^{2h} J_\Gamma^{2h}) \otimes \mathbf{I})^{-1} \tilde{\mathcal{A}}_3^{2h} \mathbf{c}^{*,n+1} \right)_i = \mathcal{R}_i \left(((\Lambda^h J_\Gamma^h) \otimes \mathbf{I})^{-1} (\mathcal{A}_3^h \mathbf{f}^{*,n+1} - h_3 \omega_1 \boldsymbol{\eta}^{*,n+1}) \right), i \in I_{\Gamma^c}.$$

- 337 • Evaluate the acceleration at all grid points

338
$$\tilde{\mathbf{a}}_c^n = \frac{\tilde{\mathbf{c}}^{*,n+1} - 2\tilde{\mathbf{c}}^n + \tilde{\mathbf{c}}^{n-1}}{\Delta_t^2}, \quad \mathbf{a}_f^n = \frac{\mathbf{f}^{*,n+1} - 2\mathbf{f}^n + \mathbf{f}^{n-1}}{\Delta_t^2}.$$

- 339 • Compute the corrector at the interior grid points

340
$$\mathbf{c}_i^{n+1} = \mathbf{c}_i^{*,n+1} + \frac{\Delta_t^4}{12} ((\rho^{2h} \otimes \mathbf{I})(J^{2h} \otimes \mathbf{I}))^{-1} \hat{\mathcal{L}}_i^{2h} \mathbf{a}_c^n, \quad i \in I_{\Omega^c},$$

342
$$\mathbf{f}_i^{n+1} = \mathbf{f}_i^{*,n+1} + \frac{\Delta_t^4}{12} ((\rho^h \otimes \mathbf{I})(J^h \otimes \mathbf{I}))^{-1} \hat{\mathcal{L}}_i^h \mathbf{a}_f^n, \quad i \in I_{\Omega^f}.$$

- 343 • At the interface Γ , the values \mathbf{f}_i^{n+1} are computed by the continuity of solution

344
$$\mathbf{f}_i^{n+1} = \mathcal{P}_i(\mathbf{c}_i^{n+1}), \quad i \in I_{\Gamma^f}.$$

- 345 • At the interface Γ , the ghost point values in $\tilde{\mathbf{c}}^{n+1}$ are computed by solving the equation for the
 346 continuity of traction

347 (4.2)
$$\left(((\Lambda^{2h} J_\Gamma^{2h}) \otimes \mathbf{I})^{-1} \tilde{\mathcal{A}}_3^{2h} \mathbf{c}^{n+1} \right)_i = \mathcal{R}_i \left(((\Lambda^h J_\Gamma^h) \otimes \mathbf{I})^{-1} (\mathcal{A}_3^h \mathbf{f}^{n+1} - h_3 \omega_1 \boldsymbol{\eta}^{n+1}) \right), \quad i \in I_{\Gamma^c}.$$

348
 349
 350 In the Algorithm 4.1, we need to solve the linear systems for the continuity of traction at the interface
 351 Γ in both predictor step (4.1) and corrector step (4.2). The linear system matrices of (4.1) and (4.2) are
 352 the same. Therefore, we only present how to solve (4.1) in the predictor step.

353 There are $3n_1^{2h} n_2^{2h}$ unknowns and $3n_1^{2h} n_2^{2h}$ linear equations in (4.1). For large problems in three
 354 dimensions, it is very memory inefficient to calculate the LU-factorization. Therefore, we use iterative
 355 methods to solve the linear system in (4.1). In particular, we consider three different iterative methods:
 356 the block Jacobi iterative method, the conjugate gradient (CG) iterative method and the preconditioned
 357 conjugate gradient iterative method. The detailed methods and a comparison are given in Section 5.2.

358 **5. Numerical Experiments.** We present four numerical experiments. In Sec. 5.1, we verify the
 359 order of the convergence of the proposed scheme (3.7, 3.15, 3.11, 3.16). In Sec. 5.2, we present three
 360 iterative methods for solving the linear systems (4.1) and (4.2). The efficiency of the iterative methods is
 361 investigated and a comparison with the LU-factorization method is conducted. Next, in Sec. 5.3 we show
 362 that our scheme does not generate any reflections at the mesh refinement interface. Finally, the energy
 363 conservation property is verified in Sec. 5.4 with heterogeneous and discontinuous material properties.

364 **5.1. Verification of convergence rate.** We use the method of the manufactured solution to verify
 365 the fourth order convergence rate of the proposed scheme. We choose the mapping of the coarse domain
 366 Ω^c as

$$367 \quad \mathbf{x} = \mathbf{X}^c(\mathbf{r}) = \begin{pmatrix} 2\pi r^{(1)} \\ 2\pi r^{(2)} \\ r^{(3)}\theta_i(r^{(1)}, r^{(2)}) + (1 - r^{(3)})\theta_b(r^{(1)}, r^{(2)}) \end{pmatrix},$$

368 where $0 \leq r^{(1)}, r^{(2)}, r^{(3)} \leq 1$, θ_i represents the interface surface geometry,

$$369 \quad (5.1) \quad \theta_i(r^{(1)}, r^{(2)}) = \pi + 0.2 \sin(4\pi r^{(1)}) + 0.2 \cos(4\pi r^{(2)}),$$

370 and θ_b is the bottom surface geometry,

$$371 \quad \theta_b(r^{(1)}, r^{(2)}) = 0.2 \exp\left(-\frac{(r^{(1)} - 0.6)^2}{0.04}\right) + 0.2 \exp\left(-\frac{(r^{(2)} - 0.6)^2}{0.04}\right).$$

372 As for the fine domain Ω^f , the mapping is chosen to be

$$373 \quad \mathbf{x} = \mathbf{X}^f(\mathbf{r}) = \begin{pmatrix} 2\pi r^{(1)} \\ 2\pi r^{(2)} \\ r^{(3)}\theta_t(r^{(1)}, r^{(2)}) + (1 - r^{(3)})\theta_i(r^{(1)}, r^{(2)}) \end{pmatrix},$$

374 where $0 \leq r^{(1)}, r^{(2)}, r^{(3)} \leq 1$ and θ_t is the top surface geometry,

$$375 \quad \theta_t(r^{(1)}, r^{(2)}) = 2\pi + 0.2 \exp\left(-\frac{(r^{(1)} - 0.5)^2}{0.04}\right) + 0.2 \exp\left(-\frac{(r^{(2)} - 0.5)^2}{0.04}\right).$$

376 In the entire domain, we choose the density

$$377 \quad \rho(x^{(1)}, x^{(2)}, x^{(3)}) = 2 + \sin(x^{(1)} + 0.3) \sin(x^{(2)} + 0.3) \sin(x^{(3)} - 0.2),$$

378 and material parameters μ, λ

$$379 \quad \mu(x^{(1)}, x^{(2)}, x^{(3)}) = 3 + \sin(3x^{(1)} + 0.1) \sin(3x^{(2)} + 0.1) \sin(x^{(3)}),$$

380 and

$$381 \quad \lambda(x^{(1)}, x^{(2)}, x^{(3)}) = 21 + \cos(x^{(1)} + 0.1) \cos(x^{(2)} + 0.1) \sin^2(3x^{(3)}).$$

382 In addition, we impose a boundary forcing on the top surface and Dirichlet boundary conditions for
 383 the other boundaries. The external forcing, top boundary forcing \mathbf{g} and initial conditions are chosen
 384 such that the solutions for both fine domain (\mathbf{F}) and coarse domain (\mathbf{C}) are $\mathbf{F}(\cdot, t) = \mathbf{C}(\cdot, t) = \mathbf{u}(\cdot, t) =$
 385 $(u_1(\cdot, t), u_2(\cdot, t), u_3(\cdot, t))^T$ with

$$386 \quad u_1(\cdot, t) = \cos(x^{(1)} + 0.3) \sin(x^{(2)} + 0.3) \sin(x^{(3)} + 0.2) \cos(t^2),$$

$$387 \quad u_2(\cdot, t) = \sin(x^{(1)} + 0.3) \cos(x^{(2)} + 0.3) \sin(x^{(3)} + 0.2) \cos(t^2),$$

$$388 \quad u_3(\cdot, t) = \sin(x^{(1)} + 0.2) \sin(x^{(2)} + 0.2) \cos(x^{(3)} + 0.2) \sin(t).$$

390 For example, for the boundary forcing at the top surface, we have

$$391 \quad \mathbf{g} = (g_1, g_2, g_3)^T = \sum_{i=1}^3 \left(\sum_{j=1}^3 M_{ij}^f \frac{\partial \mathbf{u}}{\partial x^{(j)}} \right) n_3^{f,+i},$$

392 where, M_{ij}^f and $n_3^{f,+i}$ are defined in (2.4) and (2.5), respectively.

393 The problem is evolved until final time $T = 0.5$. In Table 1, we use L_2 to represent the L^2 error in
394 the entire domain $\Omega = \Omega^c \cup \Omega^f$. The notations L_2^f and L_2^c represent the L^2 error in the fine domain Ω^f
395 and coarse domain Ω^c , respectively. The convergence rates are shown in the parentheses in Table 1. We
396 observe that the convergence rate is fourth order for all cases. Even though the boundary accuracy of
397 the SBP operator is only second order, the optimal convergence rate is fourth order. For a more detailed
398 analysis of the convergence rate, we refer to [15, 16]. To solve the linear system for ghost point values,
399 we use a block Jacobi iterative method. In the following section, we study two more iterative methods
400 and compare them in terms of the condition number and the number of iterations.

$2h_1 = 2h_2 = 2h_3 = 2h$	L_2	L_2^f	L_2^c
$2\pi/24$	2.2227e-03	8.0442e-04	2.0720e-03
$2\pi/48$	1.4142e-04 (3.97)	5.1478e-05 (3.97)	1.3171e-04 (3.98)
$2\pi/96$	8.6166e-06 (4.04)	3.0380e-06 (4.08)	8.0632e-06 (4.03)

TABLE 1

The L^2 error and corresponding convergence rates of the fourth order SBP method

401 **5.2. Iterative methods.** In this section, we use the same example as in Sec. 5.1. For the proposed
402 scheme (3.7, 3.15, 3.11, 3.16), we need to solve linear systems with $3n_1^{2h}n_2^{2h}$ unknown ghost point values on
403 the coarse grid. At each time step, two linear systems with the same matrix are solved for the continuity
404 of traction at the interface Γ .

405 We investigate three iterative methods: the block Jacobi method, the conjugate gradient method and
406 the preconditioned conjugate gradient method. We note that the coefficient matrix of the linear system
407 arising from the continuity of traction at interface Γ is not symmetric for this test problem. However, our
408 experiment shows that both the conjugate gradient method and the preconditioned conjugate gradient
409 method converge.

410 For the problem proposed in Sec. 5.1, the structure of the coefficient matrix of the linear system
411 arising in (3.16) is shown in Figure 5, which is determined by the interpolation operator \mathcal{P} and restriction
412 operator \mathcal{R} . In this example, we use $n_1^{2h} = n_2^{2h} = 13$, $n_3^{2h} = 7$. We choose the entries indicated by red color
413 in Figure 5 to be the block Jacobi matrix in the block Jacobi iterative method and the preconditioning
414 matrix in the preconditioned conjugate gradient method. The absolute error tolerance is set to be 10^{-7}
415 for all three iterative methods and $h_1 = h_2 = h_3 = h$.

$2h$	CG	Block Jacobi	Preconditioned CG
$2\pi/24$	37.78	24.96	4.01
$2\pi/48$	38.61	25.38	2.87
$2\pi/96$	39.14	25.43	2.25

TABLE 2

The condition number of the matrices in the conjugate gradient method, the block Jacobi method and the preconditioned conjugate gradient method

416 Table 2 shows the condition number of the original coefficient matrix, the block Jacobi matrix and
417 the coefficient matrix after applying the preconditioning matrix. We observe that the condition number
418 for preconditioned conjugate gradient method is smallest and is consistent with the results of iteration
419 number for different iterative methods: there are around 44 iterations for the conjugate gradient method,
420 13 iterations for the block Jacobi method and 9 iterations for the preconditioned conjugate gradient
421 method.

422 In comparison, we have also performed an LU factorization for the linear system when the mesh size
 423 $2h = 2\pi/96$, and the computation takes 40.6 GB memory. In contrast, with the block Jacobi method,
 424 the peak memory usage is only 1.2 GB. For large-scale problems, the memory usage becomes infeasible
 425 for the LU factorization.

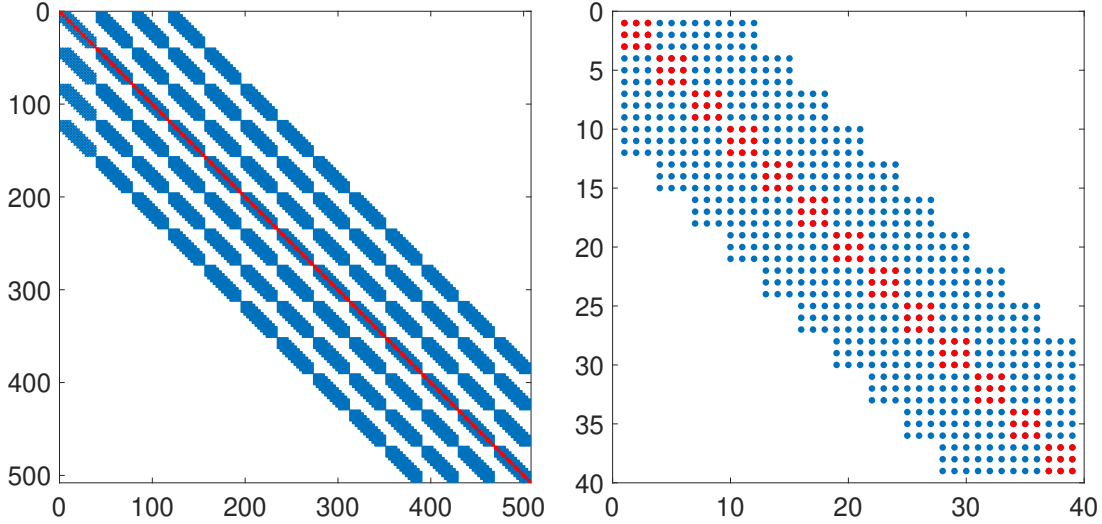


FIG. 5. The left panel is the structure of the coefficient matrix of the linear system (3.16). The right panel shows a close-up of one diagonal block.

426 **5.3. Gaussian source.** In this section, we perform a numerical simulation with a Gaussian source
 427 at the top surface and verify that the curved mesh refinement interface does not generate any artifacts.
 428 We choose a flat top and bottom surface geometry

$$429 \quad \theta_t(r^{(1)}, r^{(2)}) = 1000, \quad \theta_b(r^{(1)}, r^{(2)}) = 0,$$

430 respectively. The mesh refinement interface is parameterized by

$$431 \quad (5.2) \quad \theta_i(r^{(1)}, r^{(2)}) = 800 + 20 \sin(4\pi r^{(1)}) + 20 \cos(4\pi r^{(2)}),$$

432 where $0 \leq r^{(1)}, r^{(2)}, r^{(3)} \leq 1$. In addition, the mapping in the coarse domain Ω^c and fine domain Ω^f are
 433 given by

$$434 \quad \mathbf{x} = \mathbf{X}^c(\mathbf{r}) = \begin{pmatrix} 2000r^{(1)} \\ 2000r^{(2)} \\ r^{(3)}\theta_i(r^{(1)}, r^{(2)}) + (1 - r^{(3)})\theta_b(r^{(1)}, r^{(2)}) \end{pmatrix}$$

435 and

$$436 \quad \mathbf{x} = \mathbf{X}^f(\mathbf{r}) = \begin{pmatrix} 2000r^{(1)} \\ 2000r^{(2)} \\ r^{(3)}\theta_t(r^{(1)}, r^{(2)}) + (1 - r^{(3)})\theta_i(r^{(1)}, r^{(2)}) \end{pmatrix},$$

437 respectively. In the entire domain, we use the homogeneous material properties

$$438 \quad \rho(x^{(1)}, x^{(2)}, x^{(3)}) = 1.5 \times 10^3, \quad \mu(x^{(1)}, x^{(2)}, x^{(3)}) = 1.5 \times 10^9, \quad \lambda(x^{(1)}, x^{(2)}, x^{(3)}) = 3 \times 10^9.$$

439 At the top surface, the Gaussian source $\mathbf{g} = (g_1, g_2, g_3)^T$ is imposed as the Dirichlet data with
 440 $g_1 = g_2 = 0$ and

$$441 \quad g_3 = 10^9 \exp \left(- \left(\frac{t - 4/44.2}{1/44.2} \right)^2 \right) \exp \left(- \left(\frac{x^{(1)} - 1000}{12.5} \right)^2 - \left(\frac{x^{(2)} - 1000}{12.5} \right)^2 \right).$$

442 Homogeneous Dirichlet boundary conditions are imposed at other boundaries. Both the initial conditions
 443 and the external forcing are set to zero everywhere. For these material properties, the shear wave velocity
 444 is $c_s = \sqrt{\mu/\rho} = 1000$. With the dominant wave frequency $f_0 = 44.2\sqrt{2}/(2\pi) \approx 10$, the corresponding
 445 wavelength c_s/f_0 is approximately 100.

446 In the numerical schemes, we consider three different meshes: Mesh 1 is the Cartesian mesh without
 447 any interface and $n_1 = n_2 = 201, n_3 = 101$ with n_i denotes the number of grid points in the direction $x^{(i)}$.
 448 This corresponds to 10 grid points per wavelength and is considered as the reference solution. Mesh 2 is the
 449 curvilinear mesh with a curved mesh refinement interface defined in (5.2) and $n_1^{2h} = n_2^{2h} = 101, n_3^{2h} = 41$,
 450 $n_1^h = n_2^h = 201, n_3^h = 21$. The mesh size in Ω^f is approximately the same as the mesh size in the Cartesian
 451 mesh. As a result, the waves are resolved with 5 grid points per wavelength in Ω^c . Mesh 3 is obtained
 452 by refining Mesh 2 in all three spatial directions.

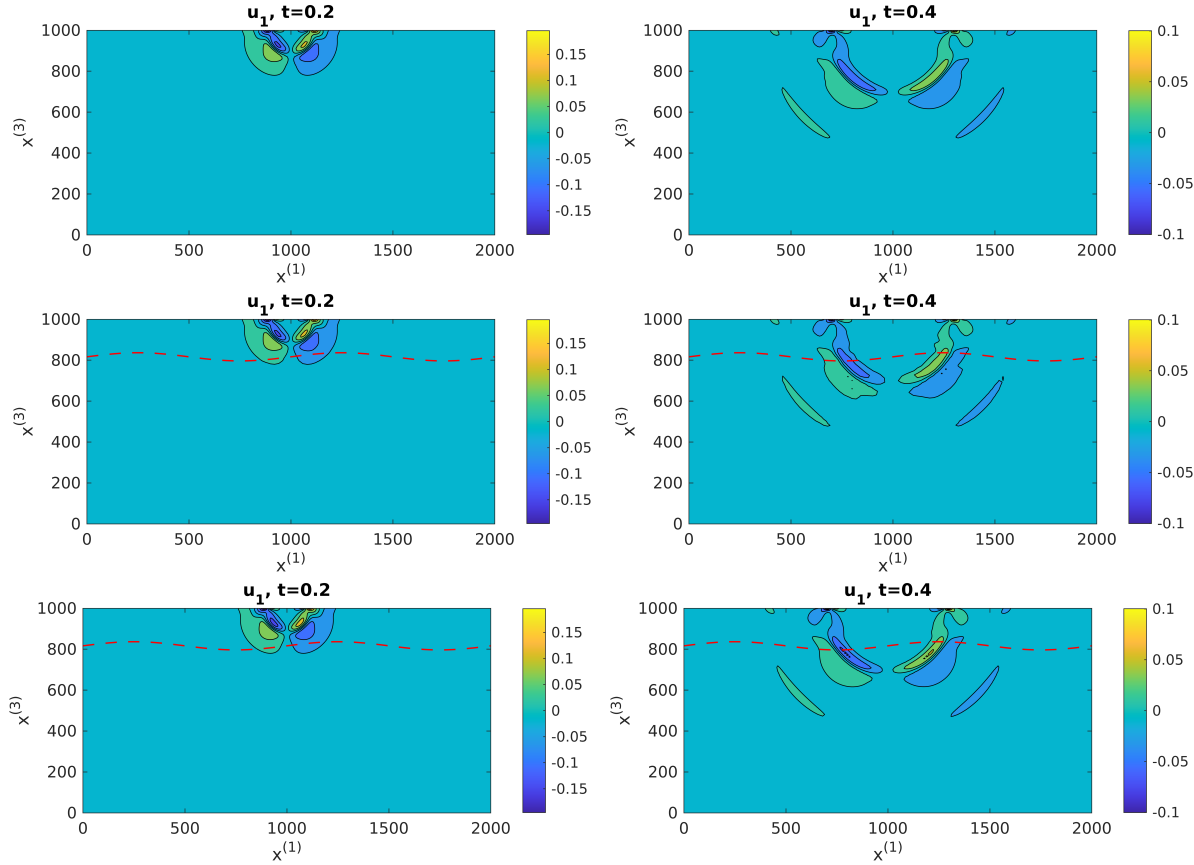


FIG. 6. The graphs for u_1 . In the top, middle and bottom panel, we show numerical solutions at $t = 0.2$ and $t = 0.4$ computed with Mesh 1, Mesh 2 and Mesh 3, respectively. The curved interfaces are marked with the red dash lines.

453 In Figure 6, we plot the component u_1 at $t = 0.2$ and $t = 0.4$. Some artifacts are observed in the
 454 solution computed with the second mesh, which is due to the small number of grid points per wavelength
 455 in Ω^c . The results become better when the finer curvilinear mesh is used. From Figure 7, we observe
 456 that there is no obvious reflection at the mesh refinement interface for the component u_3 , and we have a
 457 better results when a finer curvilinear mesh is used. The component u_2 is zero up to round-off error for
 458 both the Cartesian mesh and curvilinear meshes and is not presented here.

459 **5.4. Energy conservation test.** To verify the energy conservation property of the scheme, we
 460 perform computation without external source term, but with a Gaussian initial data centered at the
 461 origin of the computational domain. The computational domain is chosen to be the same as in Sec. 5.1.
 462 The material property is heterogeneous and discontinuous: for the fine domain Ω^f , the density varies

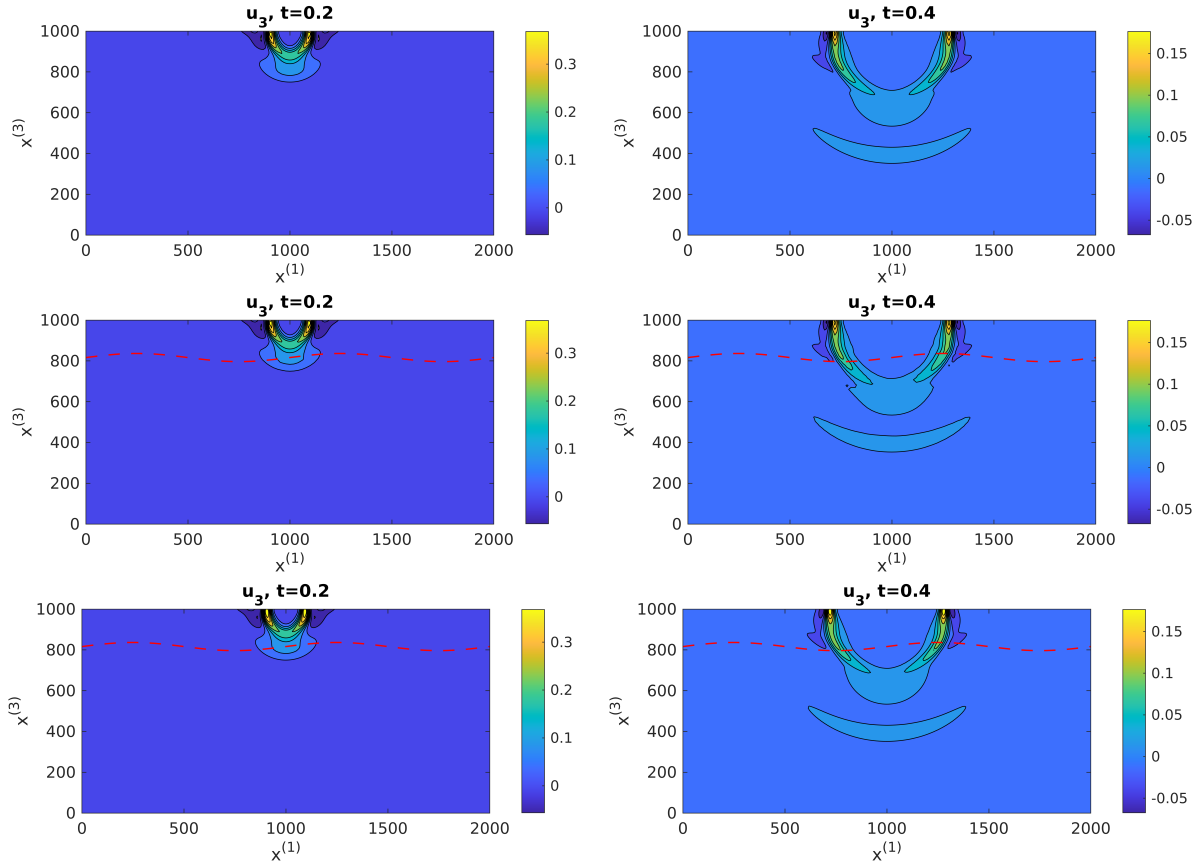


FIG. 7. The graphs for u_3 . In the top, middle and bottom panel, we show numerical solutions at $t = 0.2$ and $t = 0.4$ computed with Mesh 1, Mesh 2 and Mesh 3, respectively. The curved interfaces are marked with the red dash lines.

463 according to

$$464 \quad \rho^f(x^{(1)}, x^{(2)}, x^{(3)}) = 3 + \sin(2x^{(1)} + 0.3) \cos(x^{(2)} + 0.3) \sin(2x^{(3)} - 0.2),$$

465 and material parameters satisfy

$$466 \quad \mu^f(x^{(1)}, x^{(2)}, x^{(3)}) = 2 + \cos(3x^{(1)} + 0.1) \sin(3x^{(2)} + 0.1) \sin(x^{(3)})^2,$$

467

$$468 \quad \lambda^f(x^{(1)}, x^{(2)}, x^{(3)}) = 15 + \cos(x^{(1)} + 0.1) \sin(4x^{(2)} + 0.1) \sin(3x^{(3)})^2;$$

469 for the coarse domain Ω^c , the density varies according to

$$470 \quad \rho^c(x^{(1)}, x^{(2)}, x^{(3)}) = 2 + \sin(x^{(1)} + 0.3) \sin(x^{(2)} + 0.3) \sin(2x^{(3)} - 0.2),$$

471 and material parameters satisfy

$$472 \quad \mu^c(x^{(1)}, x^{(2)}, x^{(3)}) = 3 + \sin(3x^{(1)} + 0.1) \sin(3x^{(2)} + 0.1) \sin(x^{(3)}),$$

473

$$474 \quad \lambda^c(x^{(1)}, x^{(2)}, x^{(3)}) = 21 + \cos(x^{(1)} + 0.1) \cos(x^{(2)} + 0.1) \sin(3x^{(3)})^2.$$

475 The initial Gaussian data is given by $\mathbf{C}(\cdot, 0) = \mathbf{F}(\cdot, 0) = \mathbf{u}(\cdot, 0) = (u_1(\cdot, 0), u_2(\cdot, 0), u_3(\cdot, 0))^T$ with

476
$$u_1(\cdot, 0) = \exp\left(-\frac{(x^{(1)} - \pi)^2}{0.1}\right) \exp\left(-\frac{(x^{(2)} - \pi)^2}{0.1}\right) \exp\left(-\frac{(x^{(3)} - \pi)^2}{0.1}\right),$$

477
$$u_2(\cdot, 0) = \exp\left(-\frac{(x^{(1)} - \pi)^2}{0.2}\right) \exp\left(-\frac{(x^{(2)} - \pi)^2}{0.2}\right) \exp\left(-\frac{(x^{(3)} - \pi)^2}{0.2}\right),$$

478
$$u_3(\cdot, 0) = \exp\left(-\frac{(x^{(1)} - \pi)^2}{0.1}\right) \exp\left(-\frac{(x^{(2)} - \pi)^2}{0.2}\right) \exp\left(-\frac{(x^{(3)} - \pi)^2}{0.2}\right).$$

480 The grid spacing in the parameter space for the coarse domain Ω^c is $2h_1 = 2h_2 = 2h_3 = \frac{\pi}{24}$ and for the
481 fine domain Ω^f is $h_1 = h_2 = h_3 = \frac{\pi}{48}$, that is we have $25 \times 25 \times 13$ grid points in the coarse domain Ω^c
482 and $49 \times 49 \times 25$ grid points in the fine domain Ω^f .

483 The semi-discrete energy is given by $(\mathbf{f}_t, (\rho^h \otimes \mathbf{I})\mathbf{f}_t)_h + \mathcal{S}_h(\mathbf{f}, \mathbf{f}) + (\mathbf{c}_t, (\rho^{2h} \otimes \mathbf{I})\mathbf{c}_t)_{2h} + \mathcal{S}_{2h}(\mathbf{c}, \mathbf{c})$, see
484 (3.27). By using the same approach as for the isotropic elastic wave equation, see [11, 12], the expression
485 for the fully discrete energy reads

486
$$E^{n+1/2} = \left\| (\rho^h \otimes \mathbf{I})^{\frac{1}{2}} \frac{\mathbf{f}^{n+1} - \mathbf{f}^n}{\Delta t} \right\|_h^2 + S_h(\mathbf{f}^{n+1}, \mathbf{f}^n) - \frac{(\Delta t)^2}{12} \left((J^h \otimes \mathbf{I})^{-1} \mathcal{L}^h \mathbf{f}^{n+1}, (J^h \otimes \mathbf{I})^{-1} \mathcal{L}^h \mathbf{f}^n \right)_h$$

487
$$+ \left\| (\rho^{2h} \otimes \mathbf{I})^{\frac{1}{2}} \frac{\mathbf{c}^{n+1} - \mathbf{c}^n}{\Delta t} \right\|_{2h}^2 + S_{2h}(\mathbf{c}^{n+1}, \mathbf{c}^n) - \frac{(\Delta t)^2}{12} \left((J^{2h} \otimes \mathbf{I})^{-1} \tilde{\mathcal{L}}^{2h} \mathbf{c}^{n+1}, (J^{2h} \otimes \mathbf{I})^{-1} \tilde{\mathcal{L}}^{2h} \mathbf{c}^n \right)_{2h}.$$

489 We plot the relative change in the fully discrete energy, $(E^{n+1/2} - E^{1/2})/E^{1/2}$, as a function of time with
490 $t \in [0, 120]$ in Figure 8. This corresponds to 6186 time steps. Clearly, the fully discrete energy remains
491 constant up to the round-off error.

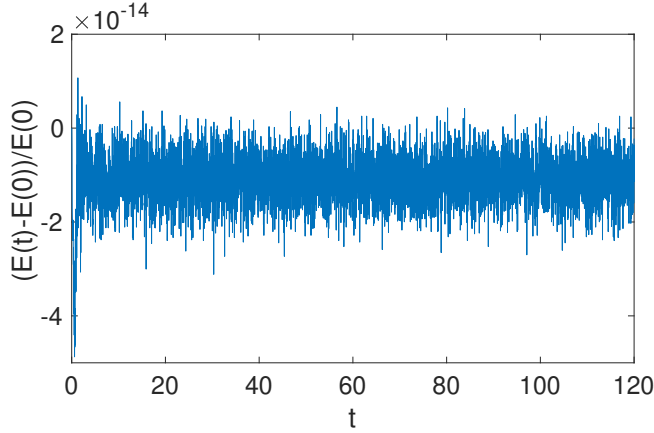


FIG. 8. The relative change in the fully discrete energy as a function of time. Here, $t = 120$ corresponds to 6186 time steps.

491

492 **6. Conclusion.** We have developed a fourth order accurate finite difference method for the three
493 dimensional elastic wave equations in heterogeneous media. To take into account discontinuous mate-
494 rial properties, we partition the domain into subdomains such that interfaces are aligned with material
495 discontinuities such that the material property is smooth in each subdomain. Adjacent subdomains are
496 coupled through physical interface conditions: continuity of displacements and continuity of traction.

497 In a realistic setting, these subdomains have curved faces. We use a coordinate transformation
498 and discretize the governing equations on curvilinear meshes. In addition, we allow nonconforming mesh
499 refinement interfaces such that the mesh sizes in each block need not to be the same. With this important
500 feature, we can choose the mesh sizes according to the velocity structure of the material and keep the
501 grid points per wavelength almost the same in the entire domain.

The finite difference discretizations satisfy a summation-by-parts property. At the interfaces, physical interface conditions are imposed by using ghost points and mesh refinement interfaces with hanging nodes are treated numerically by the fourth order interpolation operators. Together with a fourth order accurate predictor-corrector time stepping method, the fully discrete equation is energy conserving. We have conducted numerical experiments to verify the energy conserving property, and the fourth order convergence rate. Furthermore, our numerical experiments indicate that there are no artificial reflections at the interface.

To obtain values of the ghost points, a system of linear equations must be solved. In our formulation, we only use ghost points from the coarse domain, which is more efficient than the traditional approach of using ghost points from both domains. For large-scale simulations in three dimensions, the LU factorization cannot be used due to memory limitations. We have studied and compared three iterative methods for solving the linear system.

We are currently incorporating the curvilinear mesh refinement algorithm into the open source code SW4 [10]. This will enable the algorithm to be used for solving realistic seismic wave propagation problems on large parallel, distributed memory, machines.

Acknowledgement. This work was performed under the auspices of the U.S. Department of Energy by Lawrence Livermore National Laboratory under Contract DE-AC52-07NA27344. This is contribution LLNL-JRNL-810518.

Appendix A. Terms in the spatial discretization.

For the first term in (3.8), we have

$$Q_l^{2h}(N_{ll}^{2h})\mathbf{c} := \begin{pmatrix} (Q_l^{2h}(N_{ll}^{2h})\mathbf{c})_1 \\ (Q_l^{2h}(N_{ll}^{2h})\mathbf{c})_2 \\ (Q_l^{2h}(N_{ll}^{2h})\mathbf{c})_3 \end{pmatrix}, \quad (Q_l^{2h}(N_{ll}^{2h})\mathbf{c})_p = \sum_{q=1}^3 Q_l^{2h}(N_{ll}^{2h}(p, q))c^{(q)}, \quad p = 1, 2, 3,$$

where we have used a matlab notation $N_{ll}^{2h}(p, q)$ to represent the p -th row and q -th column of the matrix N_{ll}^{2h} ; $Q_l^{2h}(N_{ll}^{2h}(p, q))c^{(q)}$ is the central difference operator in direction $r^{(l)}$ for spatial second derivative with variable coefficient. For the second term in (3.8), we have

$$\tilde{G}_3^{2h}(N_{33}^{2h})\mathbf{c} := \begin{pmatrix} (\tilde{G}_3^{2h}(N_{33}^{2h})\mathbf{c})_1 \\ (\tilde{G}_3^{2h}(N_{33}^{2h})\mathbf{c})_2 \\ (\tilde{G}_3^{2h}(N_{33}^{2h})\mathbf{c})_3 \end{pmatrix}, \quad (\tilde{G}_3^{2h}(N_{33}^{2h})\mathbf{c})_p = \sum_{q=1}^3 \tilde{G}_3^{2h}(N_{33}^{2h}(p, q))c^{(q)}, \quad p = 1, 2, 3,$$

where $\tilde{G}_3^{2h}(N_{33}^{2h}(p, q))c^{(j)}$ is the second derivative SBP operator defined in (3.3) for direction $r^{(3)}$. For the third term in (3.8), we have

$$D_l^{2h}(N_{lm}^{2h}D_m^{2h}\mathbf{c}) := \begin{pmatrix} (D_l^{2h}(N_{lm}^{2h}D_m^{2h}\mathbf{c}))_1 \\ (D_l^{2h}(N_{lm}^{2h}D_m^{2h}\mathbf{c}))_2 \\ (D_l^{2h}(N_{lm}^{2h}D_m^{2h}\mathbf{c}))_3 \end{pmatrix}, \quad (D_l^{2h}(N_{lm}^{2h}D_m^{2h}\mathbf{c}))_p = \sum_{q=1}^3 D_l^{2h}(N_{lm}^{2h}(p, q)D_m^{2h}c^{(q)}), \quad p = 1, 2, 3.$$

Here, $D_m^{2h}c^{(q)}$ is a central difference operator in direction $r^{(m)}$ for the spatial first derivative, and $D_3^{2h}c^{(q)}$ is the SBP operator defined in (3.1) for direction $r^{(3)}$.

For the second term in (3.10), we have

$$G_3^h(N_{33}^h)\mathbf{f} := \begin{pmatrix} (G_3^h(N_{33}^h)\mathbf{f})_1 \\ (G_3^h(N_{33}^h)\mathbf{f})_2 \\ (G_3^h(N_{33}^h)\mathbf{f})_3 \end{pmatrix}, \quad (G_3^h(N_{33}^h)\mathbf{f})_p = \sum_{q=1}^3 G_3^h(N_{33}^h(p, q))f^{(q)}, \quad p = 1, 2, 3.$$

Here, $G_3^h(N_{33}^h(p, q))f^{(q)}$ is the SBP operator defined in (3.5) for direction $r^{(3)}$.

For the continuity of traction (3.16), we have

$$\tilde{\mathcal{A}}_3^{2h}\mathbf{c} = N_{31}^{2h}D_1^{2h}\mathbf{c} + N_{32}^{2h}D_2^{2h}\mathbf{c} + N_{33}^{2h}\tilde{D}_3^{2h}\mathbf{c},$$

where

$$N_{3l}^{2h}D_l^{2h}\mathbf{c} := \begin{pmatrix} (N_{3l}^{2h}D_l^{2h}\mathbf{c})_1 \\ (N_{3l}^{2h}D_l^{2h}\mathbf{c})_2 \\ (N_{3l}^{2h}D_l^{2h}\mathbf{c})_3 \end{pmatrix}, \quad (N_{3l}^{2h}D_l^{2h}\mathbf{c})_p = \sum_{q=1}^3 N_{3l}^{2h}(p, q)D_l^{2h}c^{(q)}, \quad l = 1, 2, \quad p = 1, 2, 3$$

543 with $D_l^{2h}c^{(q)}$ to be a central difference operator for first spatial derivative in direction $r^{(l)}$, and

$$544 \quad N_{33}^{2h}\tilde{D}_3^{2h}\mathbf{c} := \begin{pmatrix} (N_{33}^{2h}\tilde{D}_3^{2h}\mathbf{c})_1 \\ (N_{33}^{2h}\tilde{D}_3^{2h}\mathbf{c})_2 \\ (N_{33}^{2h}\tilde{D}_3^{2h}\mathbf{c})_3 \end{pmatrix}, \quad (N_{33}^{2h}\tilde{D}_3^{2h}\mathbf{c})_p = \sum_{q=1}^3 N_{33}^{2h}(p, q)\tilde{D}_3^{2h}c^{(q)}, \quad p = 1, 2, 3$$

546 with $\tilde{D}_3^{2h}c^{(q)}$ to be the difference operator for first spatial derivative in direction $r^{(3)}$ defined as in the
547 second equation of (3.4); and

$$548 \quad \mathcal{A}_3^h\mathbf{f} = N_{31}^h D_1^h\mathbf{f} + N_{32}^h D_2^h\mathbf{f} + N_{33}^h D_3^h\mathbf{f},$$

549 where

$$550 \quad N_{33}^h D_3^h\mathbf{f} := \begin{pmatrix} (N_{33}^h D_3^h\mathbf{f})_1 \\ (N_{33}^h D_3^h\mathbf{f})_2 \\ (N_{33}^h D_3^h\mathbf{f})_3 \end{pmatrix}, \quad (N_{33}^h D_3^h\mathbf{f})_p = \sum_{q=1}^3 N_{33}^h(p, q)D_3^h f^{(q)}, \quad p = 1, 2, 3$$

552 with $D_3^h f^{(q)}$ to be the SBP operator for first spatial derivative in direction $r^{(3)}$ defined as in the first
553 equation of (3.6). And $N_{3l}^h D_l^h\mathbf{f}$, $l = 1, 2$ are defined similar as those in $\tilde{\mathcal{A}}_3^{2h}\mathbf{c}$.

Appendix B. Bilinear form.

The term $\mathcal{S}_{2h}(\mathbf{c}_t, \mathbf{c})$ in (3.23) is given by

$$556 \quad \mathcal{S}_{2h}(\mathbf{c}_t, \mathbf{c}) = (D_1^{2h}\mathbf{c}_t, N_{11}^{2h}D_1^{2h}\mathbf{c})_{2h} + (D_1^{2h}\mathbf{c}_t, N_{12}^{2h}D_2^{2h}\mathbf{c})_{2h} + (D_1^{2h}\mathbf{c}_t, N_{13}^{2h}D_3^{2h}\mathbf{c})_{2h} \\ 557 \quad + (D_2^{2h}\mathbf{c}_t, N_{21}^{2h}D_1^{2h}\mathbf{c})_{2h} + (D_2^{2h}\mathbf{c}_t, N_{22}^{2h}D_2^{2h}\mathbf{c})_{2h} + (D_2^{2h}\mathbf{c}_t, N_{23}^{2h}D_3^{2h}\mathbf{c})_{2h} \\ 558 \quad + (D_3^{2h}\mathbf{c}_t, N_{31}^{2h}D_1^{2h}\mathbf{c})_{2h} + (D_3^{2h}\mathbf{c}_t, N_{32}^{2h}D_2^{2h}\mathbf{c})_{2h} + (D_3^{2h}\mathbf{c}_t, N_{33}^{2h}D_3^{2h}\mathbf{c})_{2h} \\ 559 \quad + (\mathbf{c}_t, P_1^{2h}(N_{11}^{2h})\mathbf{c})_{2hr} + (\mathbf{c}_t, P_2^{2h}(N_{22}^{2h})\mathbf{c})_{2hr} + (\mathbf{c}_t, P_3^{2h}(N_{33}^{2h})\mathbf{c})_{2hr},$$

561 where $P_3^{2h}(N_{33}^{2h})$ is a positive semi-definite operator defined in (3.3) for direction $r^{(3)}$; $P_1^{2h}(N_{11}^{2h})$, $P_2^{2h}(N_{22}^{2h})$
562 are analogue to $P_3^{2h}(N_{33}^{2h})$.

563 The term $\mathcal{S}_h(\mathbf{f}_t, \mathbf{f})$ is defined as

$$564 \quad \mathcal{S}_h(\mathbf{f}_t, \mathbf{f}) = (D_1^h\mathbf{f}_t, N_{11}^h D_1^h\mathbf{f})_h + (D_1^h\mathbf{f}_t, N_{12}^h D_2^h\mathbf{f})_h + (D_1^h\mathbf{f}_t, N_{13}^h D_3^h\mathbf{f})_h \\ 565 \quad + (D_2^h\mathbf{f}_t, N_{21}^h D_1^h\mathbf{f})_h + (D_2^h\mathbf{f}_t, N_{22}^h D_2^h\mathbf{f})_h + (D_2^h\mathbf{f}_t, N_{23}^h D_3^h\mathbf{f})_h \\ 566 \quad + (D_3^h\mathbf{f}_t, N_{31}^h D_1^h\mathbf{f})_h + (D_3^h\mathbf{f}_t, N_{32}^h D_2^h\mathbf{f})_h + (D_3^h\mathbf{f}_t, N_{33}^h D_3^h\mathbf{f})_h \\ 567 \quad + (\mathbf{f}_t, P_1^h(N_{11}^h)\mathbf{f})_{hr} + (\mathbf{f}_t, P_2^h(N_{22}^h)\mathbf{f})_{hr} + (\mathbf{f}_t, P_3^h(N_{33}^h)\mathbf{f})_{hr}.$$

570 Here, $P_l^h(N_{ll}^h)$ are defined similar as $P_l^{2h}(N_{ll}^{2h})$ in $\mathcal{S}_{2h}(\mathbf{c}_t, \mathbf{c})$.

571 REFERENCES

- 572 [1] M. ALMQUIST, S. WANG, AND J. WERPERS, Order-preserving interpolation for summation-by-parts operators at
573 nonconforming grid interfaces, SIAM J. Sci. Comput., 41, pp. A1201–A1227.
- 574 [2] M. H. CARPENTER, D. GOTTLIEB, AND S. ABARBANEL, Time-stable boundary conditions for finite-difference schemes
575 solving hyperbolic systems: methodology and application to high-order compact schemes, J. Comput. Phys., 111
576 (1994), pp. 220–236.
- 577 [3] K. DURU AND K. VIRTANEN, Stable and high order accurate difference methods for the elastic wave equation in
578 discontinuous media, J. Comput. Phys., 279 (2014), pp. 37–62.
- 579 [4] T. HAGSTROM AND G. HAGSTROM, Grid stabilization of high-order one-sided differencing II: second-order wave
580 equations, J. Comput. Phys., 231 (2012), pp. 7907–7931.
- 581 [5] H. O. KREISS AND J. OLIGER, Comparison of accurate methods for the integration of hyperbolic equations, Tellus, 24
582 (1972), pp. 199–215.
- 583 [6] H. O. KREISS AND G. SCHERER, Finite element and finite difference methods for hyperbolic partial differential
584 equations, Mathematical Aspects of Finite Elements in Partial Differential Equations, Symposium Proceedings,
585 (1974), pp. 195–212.
- 586 [7] T. LUNDQUIST, A. MALAN, AND J. NORDSTRÖM, A hybrid framework for coupling arbitrary summation-by-parts
587 schemes on general meshes, J. Comput. Phys., 362 (2018), pp. 49–68.

- 588 [8] K. MATTSSON, Summation by parts operators for finite difference approximations of second-derivatives with variable
 589 coefficient, *J. Sci. Comput.*, 51 (2012), pp. 650–682.
- 590 [9] O. O'REILLY AND N. A. PETERSSON, Energy conservative SBP discretizations of the acoustic wave equation in covariant
 591 form on staggered curvilinear grids, arXiv:1907.01105, (2020).
- 592 [10] N. A. PETERSSON AND B. SJÖGREEN, User's guide to sw4, version 2.0, Tech. report LLNLSM-741439, Lawrence
 593 Livermore National Laboratory, 2016 (source code available from <http://geodynamics.org/cig>).
- 594 [11] N. A. PETERSSON AND B. SJÖGREEN, Wave propagation in anisotropic elastic materials and curvilinear coordinates
 595 using a summation-by-parts finite difference method, *J. Comput. Phys.*, 299 (2015), pp. 820–841.
- 596 [12] B. SJÖGREEN AND N. A. PETERSSON, A fourth order accurate finite difference scheme for the elastic wave equation in
 597 second order formulation, *J. Sci. Comput.*, 52 (2012), pp. 17–48.
- 598 [13] B. STRAND, Summation by parts for finite difference approximations for d/dx , *J. Comput. Phys.*, 110 (1994), pp. 47–67.
- 599 [14] J. F. THOMPSON, Z. U. WARSI, AND C. W. MASTIN, Numerical grid generation: foundations and applications, vol. 45,
 600 North-holland Amsterdam, 1985.
- 601 [15] S. WANG AND G. KREISS, Convergence of summation-by-parts finite difference methods for the wave equation, *J. Sci.*
 602 *Comput.*, 71 (2017), pp. 219–245.
- 603 [16] S. WANG, A. NISSEN, AND G. KREISS, Convergence of finite difference methods for the wave equation in two space
 604 dimensions, *Math. Comp.*, 87 (2018), pp. 2737–2763.
- 605 [17] S. WANG AND N. A. PETERSSON, Fourth order finite difference methods for the wave equation with mesh refinement
 606 interfaces, *SIAM J. Sci. Comput.*, 41 (2019), pp. A3246–A3275.